Lithos 122 (2011) 87–106

Contents lists available at ScienceDirect

Lithos

journal homepage: www.elsevier.com/locate/lithos

Multiple crust–mantle interactions for the destruction of the North China Craton: Geochemical and Sr–Nd–Pb–Hf isotopic evidence from the Longbaoshan alkaline complex

Ting-Guang Lan [a], Hong-Rui Fan [a,*], Fang-Fang Hu [a], Andrew G. Tomkins [b], Kui-Feng Yang [a], Yongsheng Liu [c]

[a] Key Laboratory of Mineral Resources, Institute of Geology and Geophysics, Chinese Academy of Sciences, Beijing 100029, China
[b] School of Geosciences, P.O. Box 28E, Monash University, Vic. 3800, Australia
[c] State Key Laboratory of Geological Processes and Mineral Resources, China University of Geosciences, Wuhan 430074, China

ARTICLE INFO

Article history:
Received 22 June 2010
Accepted 2 December 2010
Available online 13 December 2010

Keywords:
Alkaline complex
Crust–mantle interaction
Longbaoshan
Luxi Block
North China Craton

ABSTRACT

In situ zircon U–Pb ages and Hf isotopic data, major and trace elements, and Sr–Nd–Pb isotopic compositions are reported for the Longbaoshan alkaline intrusive complex in the western Shandong Province (Luxi Block), southeastern North China Craton. The Longbaoshan complex, which consists of quartz syenite, aegirine–augite syenite, hornblende syenite, monzonite, and syenodiorite, was emplaced at 129.4–131.7 Ma. The complex is characterized by high concentrations of SiO_2, $K_2O + Na_2O$, Al_2O_3, LILEs (e.g., Sr and Ba), and LREEs, and low concentrations of CaO, Fe_2O_3, MgO, and HFSEs (e.g., Nb, Ta, P and Ti). The Sr, Nd, Pb, and Hf isotopic values of this complex are similar to the nearby mafic rocks, which were derived from EM2-type lithospheric mantle, indicating that the Longbaoshan complex was mainly derived from partial melting of the EM2 source. Combined with geochemical and isotopic features, the high Nb/Ta ratios (average 19.2) of the Longbaoshan complex suggest that the EM2 source was induced by modification of crust-derived melts, which were in equilibrium with rutile-bearing eclogite. This was attributed to the subduction of the Yangtze continental crust. The presence of inherited zircons (2.51–2.64 Ga) with positive $\varepsilon_{Hf}(t)$ values (0.2–6.2) suggest that the ancient crust of the North China Craton was also involved in the formation of the Longbaoshan complex. Magma mixing modelling shows that those 10–35% crustal materials were assimilated in the complex. This complex may have experienced hornblende, apatite/monazite, and titanite crystal fractionation before emplacement in the shallow crust level. Two stages of crust–mantle interaction can be identified through the formation of the Longbaoshan complex, including (1) the lithospheric mantle was metasomatized by the melts/fluids derived from the subducted crust and then transformed into an EM2 counterpart, and (2) magma derived from the EM2 source underplated the ancient crust and assimilated the crust-derived materials. We thus propose that multiple crust–mantle interactions are the essential mechanism for the destruction of the NCC. The first intensive crust–mantle interaction was aroused by crustal subduction and was responsible for the lithospheric mantle destruction, and the second major crust–mantle interaction was induced by mantle-derived magma underplating and was responsible for the crustal activation.

1. Introduction

Over the last decades, the most important observation about the North China Craton (NCC) is that the lithosphere of the NCC considerably changed during the Phanerozoic, in which the cold and thick cratonic lithosphere (~200 km) in the Paleozoic was replaced by a hot and thin "oceanic" one (<80 km) in the Cenozoic (Griffin et al., 1998; Fan et al., 2000; Menzies et al., 1993; Xu, 2001). During this process, the stability of the coupled crust and lithospheric mantle was disturbed, and lithospheric mantle thinning as well as crustal activation were induced (Zhai, 2008), resulting in widespread voluminous magmatism and large-scale mineralization in the Mesozoic. Therefore, destruction of the NCC was proposed to describe this catastrophic change. Though mechanisms for such a change remain hotly debated, it is no doubt that crust–mantle interaction played an important role as indicated by plentiful mafic–ultramafic intrusions, lower-crustal xenoliths and peridotitic xenoliths (Gao et al., 2008; Jahn et al., 1999; Liu et al., 2008b, 2010; Wilde, et al., 2003; Xu et al., 2004a; Xu et al., 2008; Zhou et al., 2002). Models proposed for the crust–mantle interaction at this time can be divided into three groups: (1) melts originated from foundered lower crust metasomatize the overlying lithospheric mantle or asthenospheric mantle (Deng et al., 2007; Gao et al., 2004, 2008, 2009; Liu et al., 2008a; Wu et al., 2005; Xu et al., 2006, 2008); (2) melts derived from subducted continental or

* Corresponding author. Tel.: +86 10 82998218; fax: +86 10 62010846.
E-mail address: fanhr@mail.igcas.ac.cn (H.-R. Fan).

0024-4937/$ – see front matter © 2010 Elsevier B.V. All rights reserved.
doi:10.1016/j.lithos.2010.12.001

oceanic crust modify the lithospheric mantle (Li et al., 1998; Xu et al., 2004a, 2004b; Ying et al., 2004; Zhang et al., 2002, 2004, 2005a, 2005b); and (3) mantle-derived melts underplate lower crust and mix with the crust-derived melts (Chen and Zhai, 2003; Chen et al., 2004, 2005, 2008a; Yang et al., 2004, 2006, 2007a; Zhai et al., 2007). Compared with other cratons in the world, the NCC is relatively small. Thus, it is much easier for the NCC to be affected by subduction and collision of adjacent blocks (Zheng, 2009). The western part of Shandong Province (Luxi Block), being located at the southeastern margin of the NCC (Fig. 1a), is just an area that underwent strong crust–mantle interaction related to the Triassic collision between the NCC and the Yangtze Craton (YC) (Li et al., 1993).

Abundant small-scale dioritic to gabbroic intrusions, mafic dykes, mafic to intermediate volcanics, carbonatites, and alkaline rocks developed during the late Mesozoic in the Luxi Block. These rocks are enriched in large ionic lithophile elements (LILEs) and LREEs, and are depleted in high field strength elements (HFSEs) with EM1- to EM2-like Sr and Nd compositions from northwest to southeast. At least three models have been proposed for the petrogenesis of these rocks, including, (1) partial melting of the long-term enriched lithospheric mantle (Guo et al., 2001), (2) partial melting of the lithospheric mantle modified by the subducted Yangtze crust (Xu et al., 2004b; Ying et al., 2004; Zhang et al., 2002, 2005a, 2005b), and (3) partial melting of the mantle metasomatized by the foundered lower crust (Liu et al., 2008a; Qiu et al., 2005; Xu et al., 2006, 2008; Yang, 2007; Yang et al., 2005a, 2008). Previous studies have been concentrated on mafic intrusions, volcanics, and dykes, whereas alkaline rocks have been rarely researched.

Alkaline rocks are commonly produced in the extensional settings, such as post-collisional extension (Bonin et al., 1998; Liégeois et al., 1998) and intra-plate rifts or deep faults (Jung et al., 2007; Shellnutt and Zhou, 2008; Upadhyay et al., 2006), providing important information on crust–mantle interaction and the evolution of continental crust (Yang et al., 2007b and references therein). The Longbaoshan complex, one of the alkaline intrusions widely distributed in the Luxi Block, is relatively larger than other alkaline intrusions, and is composed of several types of rocks. In this paper, we report geochronological, petrological, and geochemical data of the Longbaoshan complex, in order to constrain its petrogenesis and significance to crust–mantle interaction in the southeastern NCC.

2. Geological background

The North China Craton, with an Archean core of 2.5–3.8 Ga, is the largest and oldest craton in China. Based on lithological, geochemical and metamorphic P–T–t path studies of the basement rocks, this craton can be divided into three parts (Fig. 1a): the Eastern Block, the Western Block and the Trans-North China Orogen (Zhao et al., 2001).

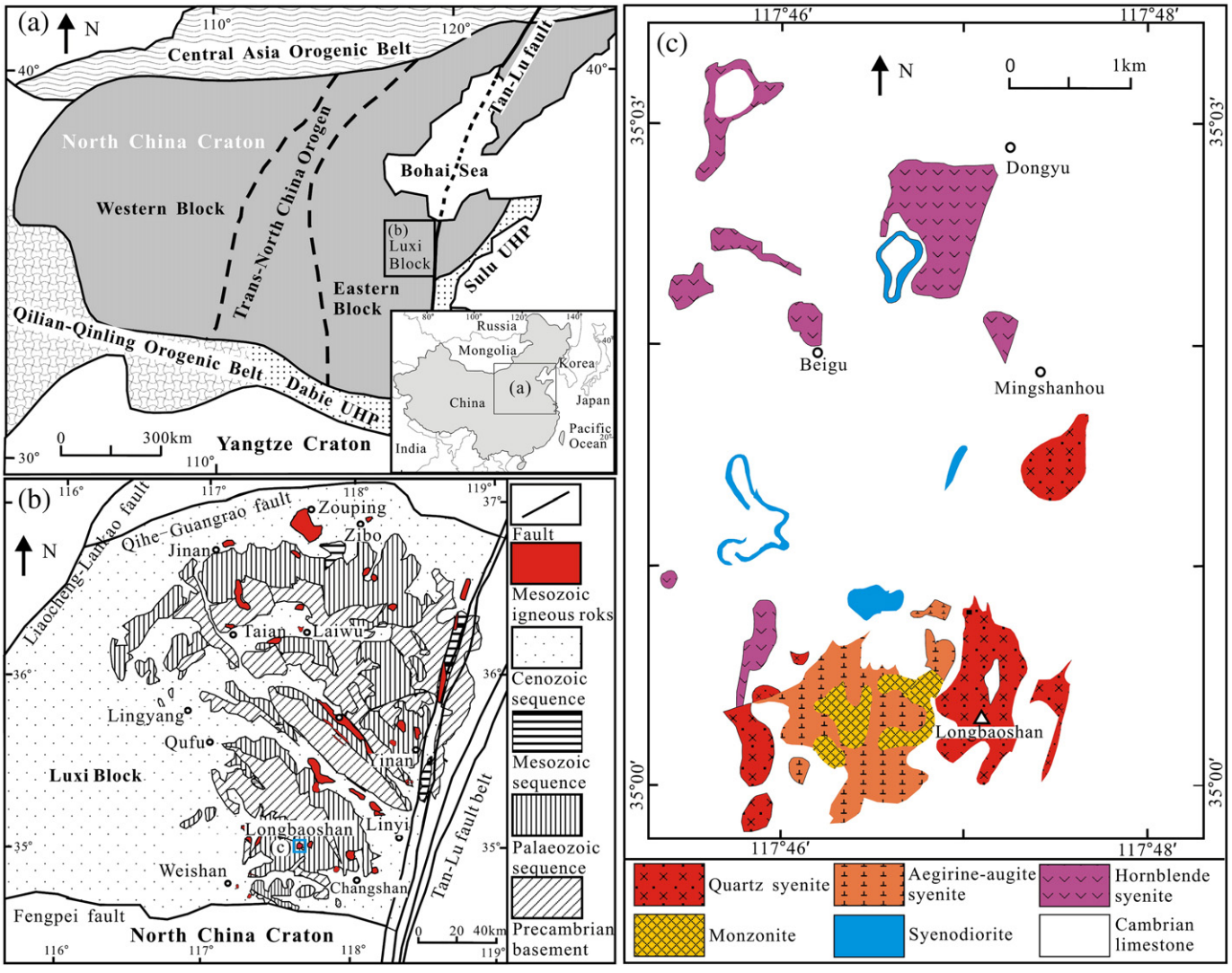

Fig. 1. (a) Simplified geological map showing the major tectonic units in eastern China and the location of Luxi Block, modified after Zhao et al. (2001) and Zhang et al. (2005a). (b) Geological map of the Luxi Block, modified after Zhang et al. (2007). (c) Geological sketch of the Longbaoshan alkaline complex.

The Eastern Block consists predominantly of late Archean tonalite–trondhjemite–granodiorite (TTG) batholiths surrounded by minor volcanic and sedimentary rocks metamorphosed from greenschist to granulite facies at ~2.5 Ga. The Western Block has a late Archean assemblage, structural style, and metamorphic history similar to that of the Eastern Block, but it differs in the absence of early to middle Archean assemblages and in being overlain by and interleaved with Paleoproterozoic khondalites. The Trans-North China Orogen, formed by the collision between the Eastern and Western Blocks during the Paleoproterozoic (1.85 Ga), is composed of late Archean to Paleoproterozoic TTG gneisses and granitoids, interleaved with abundant sedimentary and volcanic rocks (Zhao et al., 2001, 2005).

The Luxi Block is bounded by the Tan-Lu fault to the east, the Liaocheng–Lankao fault to the west, the Qihe–Guangrao fault to the north, and the Fengpei fault to the south (Zhang et al., 2007). The Tan-Lu fault, which is thought to transect the continental crust to the crust–mantle boundary (Chen et al., 2008b; Zhu et al., 2002), not only transported the eastern section of the Dabie–Sulu ultra-high pressure (UHP) metamorphic belt northwards more than 500 km (Zhu et al., 2003), but also controlled the emplacement of late Mesozoic intrusions by acting as a conduit for asthenospheric upwelling in the study area (Zhang and Dong, 2008; Zhu et al., 2003). The Sulu UHP metamorphic belt, produced by the continental collision between the NCC and the YC during the Triassic (Li et al., 1993), is about 400 km south of the Luxi Block. Late Archean gneisses, amphibolites and TTG, Paleoproterozoic granitoids, Palaeozoic carbonates interbedded with clastic rocks, Mesozoic and Cenozoic continental clastic rocks, volcaniclastics, intermediate-basic igneous rocks, mafic dykes, carbonatites, and alkaline rocks are present in the Luxi Block.

The 3.5 km^2 Longbaoshan alkaline intrusive complex intrudes into Cambrian carbonates, and consists of quartz syenite, aegirine–augite syenite, hornblende syenite, monzonite, and syenodiorite assemblages (Fig. 1c). This complex is mainly distributed in the Longbaoshan region of Cangshan County, which is about 100 km west of the Tan-Lu fault (Fig. 1b).

3. Petrography

3.1. Quartz syenite

The porphyritic quartz syenite is pale red and mainly consists of feldspar and quartz with rare biotite and accessory titanite. Feldspar crystals can be divided into three groups according to size: coarse, medium, and fine. The volumetrically dominant (50 vol.%), coarse (2–8 mm) euhedral–subhedral feldspar phenocrysts have albite cores and perthite rims. Medium-grained, euhedral–subhedral (0.5–1 mm) feldspar phenocrysts (30 vol.%) are mainly mesoperthite. The anhedral fine feldspar crystals (~0.1 mm), are mainly intergrown orthoclase and albite, and occur as a matrix phase (10–15 vol.%). Quartz phenocrysts (0.1–0.2 mm) are mainly anhedral grains (<10 vol.%). Scattered biotite crystals are small (<0.1 mm) and anhedral.

3.2. Aegirine–augite syenite

The porphyritic aegirine–augite syenite contains dominantly feldspar, with subordinate aegirine–augite, quartz, and biotite and accessory titanite and monazite. The feldspar can be divided into phenocryst and matrix phases according to size. The euhedral feldspar phenocrysts (30 vol.%) are mainly zoned albite (3.5–10 mm). The euhedral–anhedral matrix feldspars (65 vol.%), are mainly intergrown orthoclase and albite (0.5–0.1 mm). Anhedral aegirine–augite crystals (<1 vol.%) are irregular and <0.6 mm. Quartz phenocrysts (<1 vol.%) are anhedral (0.1–0.2 mm). Biotite is rare and subhedral with crystal lengths of 0.3–0.8 mm.

3.3. Hornblende syenite

The porphyritic hornblende syenite is mineralogically similar to the aegirine–augite syenite, except for the aegirine–augite and hornblende content. The hornblende syenite consists of dominantly feldspar with subordinate hornblende and quartz, and accessory magnetite. The feldspars can be divided into phenocryst and matrix phases according to size. The subhedral–anhedral (0.5–3.5 mm) feldspar phenocrysts (40 vol.%) are commonly composed of many smaller feldspar grains. Matrix feldspar (55–60 vol.%) is anhedral (0.05–0.2 mm). Euhedral–subhedral hornblende (1–5 vol.%) is usually altered to sericite or chlorite. Quartz grains (<0.1 mm) are anhedral.

3.4. Monzonite

The monzonite with red color has a porphyritic texture and a massive structure. It contains dominantly feldspar, with subordinate quartz and accessory magnetite. The feldspar crystals can be divided into phenocryst and matrix phases. Feldspar phenocrysts (2.3–4.3 mm, <1 vol.%) are mainly columnar orthoclase. Matrix feldspar (0.1–0.5 mm, 99 vol.%) is mainly subhedral–anhedral plagioclase and orthoclase. Few anhedral quartz and magnetite grains are present.

3.5. Syenodiorite

Feldspar, biotite, and hornblende are the major mineral constituents of the porphyritic syenodiorite. Feldspar can be divided into phenocryst and matrix phases according to size. The euhedral–subhedral orthoclase phenocrysts (1.5–9.0 mm, 25 vol.%) are typically composed of many smaller crystals, and have biotite and hornblende inclusions in coarser grains. Anhedral matrix plagioclase (65 vol.%) varies from 0.05 mm to 0.2 mm in size. Flaky biotite crystals (<5 vol.%) are euhedral–subhedral (0.05–1 mm). Euhedral–subhedral hornblende phenocrysts (5 vol.%) are zoned and display 56° cleavage angles, with lengths varying from 0.1 mm to 2 mm.

4. Analytical methods

Fresh rock samples were prepared in three groups: thin sections for petrography; 200 mesh powder for major, trace element, and Sr–Nd–Pb isotope analyses; 40–60 mesh crushings for selecting zircon grains to use for U–Pb dating and Hf analyses.

4.1. Cathodoluminescence (CL) images of zircon

CL images of zircon grains were obtained using a CAMECA SX50 electron microprobe at the Institute of Geology and Geophysics, Chinese Academy of Sciences (IGGCAS), in order to identify zircon internal textures and select target spots for U–Pb dating and Hf analyses. The operating conditions were 15 kV accelerating voltage and 20 nA primary beam current.

4.2. Major and trace elements

Major and trace elements were analyzed in the Major and Trace Elements Laboratories of IGGCAS, respectively. For major element analyses, mixtures of whole rock powder (0.5 g) and $Li_2B_4O_7 + LiBO_2$ (5 g) were made into glass discs and analyzed by X-ray fluorescence spectroscopy (XRF) with an AXIOS Minerals spectrometer. The analytical uncertainties were generally within 0.1–1% (RSD). For trace element analyses, whole rock powders (40 mg) were dissolved in distilled $HF + HNO_3$ in Teflon screw-cap capsules at 200 °C for 5 days, dried, and then digested with HNO_3 at 150 °C for 1 day. The final step was repeated once. Dissolved samples were diluted to 49 ml with 1% HNO_3 and 1 ml 500 ppb indium was added to the solution as an internal standard. Trace element abundances were determined by

inductively coupled plasma mass spectrometry (ICP-MS) using a Finnigan MAT Element spectrometer, which has analytical uncertainties within 5% for most elements.

4.3. Sr, Nd and Pb isotopes

Whole rock powders for Sr and Nd isotopic analyses were dissolved in Teflon bombs after being spiked with ^{87}Rb, ^{84}Sr, ^{149}Sm and ^{150}Nd tracers prior to $HF+HNO_3+HClO_4$ dissolution. Rb, Sr, Sm and Nd were separated using conventional ion exchange procedures and measured using a Finnigan MAT262 multi-collector mass spectrometer at IGGCAS. Detailed descriptions of the analytical techniques have been documented in Chu et al. (2009). Procedural blanks are <100 pg for Sm and Nd and <300 pg for Rb and Sr. The isotopic ratios were corrected for mass fractionation by normalizing to $^{86}Sr/^{88}Sr=0.1194$ and $^{146}Nd/^{144}Nd=0.7219$, respectively. The measured values for the JNdi-1 Nd standard and NBS987 Sr standard were $^{143}Nd/^{144}Nd=0.512118\pm12$ (2σ, n=10) and $^{87}Sr/^{86}Sr=0.710257\pm12$ (2σ, n=10), respectively. USGS reference material BCR-2 was measured to monitor the accuracy of the analytical procedures, with the following results: $^{143}Nd/^{144}Nd=0.512633\pm13$ (2σ, n=12) and $^{87}Sr/^{86}Sr=0.705035\pm12$ (2σ, n=12).

For Pb isotope determination, the whole rock powders were dissolved in Teflon vials with purified $HF+HNO_3$ at 120 °C for 7 days and then separated using anion-exchange columns with diluted HBr as elutant. Isotopic ratios were also measured by the Finnigan MAT262 multi-collector mass spectrometer in IGGCAS. Repeated analyses of Pb isotope standard NBS981 yielded $^{206}Pb/^{204}Pb=16.890\pm0.013$, $^{207}Pb/^{204}Pb=15.426\pm0.014$ and $^{208}Pb/^{204}Pb=36.514\pm0.014$. Relative to the following values for NBS981: $^{206}Pb/^{204}Pb=16.941$, $^{207}Pb/^{204}Pb=15.496$ and $^{208}Pb/^{204}Pb=36.722$ (Galer and Abouchami, 1998), Pb isotopic data in samples were corrected for mass fractionation of 0.15% per atomic mass unit for $^{206}Pb/^{204}Pb$, $^{207}Pb/^{204}Pb$ and $^{208}Pb/^{204}Pb$.

4.4. Zircon U–Pb dating and in situ Hf isotopic analyses

U–Pb dating and trace element analyses of zircon were conducted synchronously by LA–ICP-MS at the State Key Laboratory of Geological Processes and Mineral Resources, China University of Geosciences, Wuhan. Detailed operating conditions for the laser ablation system, the ICP-MS instrument, and the data reduction process are described by Liu et al. (2008c, 2010). Laser sampling was performed using a GeoLas 2005. An Agilent 7500a ICP-MS instrument was used to acquire ion-signal intensities. Each analysis incorporated a background acquisition of approximately 20–30 s (gas blank) followed by 50 s data acquisition from the sample. The Agilent Chemstation was utilized for the acquisition of each individual analysis. Off-line selection and integration of background and analyte signals, time–drift correction, and quantitative calibration for trace element analyses and U–Pb dating were performed by *ICPMSDataCal* (Liu et al., 2008c, 2010).

Zircon 91500 was used as the external standard for U–Pb dating, and was analyzed twice every 5 analyses. Time-dependent drifts of U–Th–Pb isotopic ratios were corrected using a linear interpolation (with time) for every five analyses according to the variations of 91500 (i.e., 2 zircon 91500 + 5 samples + 2 zircon 91500) (Liu et al., 2010). Preferred U–Th–Pb isotopic ratios used for 91500 are from Wiedenbeck et al. (1995). Uncertainty of preferred values for the external standard 91500 was propagated to the ultimate results of the samples. Concordia diagrams and weighted mean calculations were made using Isoplot/Ex ver3 (Ludwig, 2003). Trace element compositions of zircons were calibrated against reference material of GSE-1G combined with internal standardization (Liu et al., 2010). The preferred values of element concentrations for the GSE-1G reference glass are from the GeoReM database (http://georem.mpch-mainz.gwdg.de/).

In situ zircon Hf isotopic analyses were conducted on the same spots which had been analyzed for U–Pb dating. Hf isotopic compositions were determined by a Neptune MC–ICP-MS equipped with a GeolasPlus 193 nm ArF excimer laser at the IGGCAS. Laser spot size of 40 μm and laser repetition of 8 Hz with energy density of 15 J/cm^2 were used during the analyses. The signal collection model is one block with 200 cycles. Each cycle has 0.131 s integration time and total time is about 26 s during each analyses. Zircon 91500 was used as external standard for Hf isotopic analyses and was analyzed twice every 5 analyses. Repeated analyses of 91500 yielded a mean $^{176}Hf/^{177}Hf$ ratio of 0.282300 ± 24 (2σ, n=82), which is consistent with the $^{176}Hf/^{177}Hf$ ratios measured by Goolaerts et al. (2004). Detailed analytical procedures were described by Xie et al. (2008).

5. Results

5.1. Geochronology

5.1.1. Quartz syenite

Zircon crystals in the quartz syenite (Sample 07SD75) are euhedral–subhedral and range from 200 to 500 μm in size, with ratios of length to width from 1.5:1 to 2.5:1. Most grains are transparent to light maroon in color and have oscillatory zoning in the cores. Some grains have circular or irregular cores mantled by euhedral overgrowths that also have oscillatory zoning (Fig. 2a). All 18 zircons analyzed are concordant and yield a mean $^{206}Pb/^{238}U$ age of 129.4 ± 0.7 Ma (2σ) (Fig. 2b and Table 1).

5.1.2. Aegirine–augite syenite

Zircon crystals in the aegirine–augite syenite (Sample 07SD73) are euhedral and range from 350 to 800 μm in size, with length to width ratios of 2:1 to 2.5:1. Most grains are transparent to light maroon in color and have wide oscillatory zoning in the cores and narrow oscillatory zoning in the rims (Fig. 2a). The twenty analyses except one are concordant and yield a mean $^{206}Pb/^{238}U$ age of 130.1 ± 1.7 Ma (2σ) (Fig. 2c and Table 1).

5.1.3. Hornblende syenite

Zircon crystals in the hornblende syenite (Sample 08LX56) can be divided into two types: the first type are euhedral to subhedral, maroon in color, range from 100 to 300 μm in size, have mostly dark CL images, and have wide oscillatory zoning; the second type are granular and rounded and are grey with indistinct oscillatory zoning in CL images (Fig. 2a). Eighteen analyses of the first type are concordant and yield a mean $^{206}Pb/^{238}U$ age of 130.7 ± 1.0 Ma (2σ). Six analyses of the second type yield $^{207}Pb/^{206}Pb$ ages of 2517–2639 Ma, indicating that late Archean inherited zircons also exist in the hornblende syenite (Fig. 2d and Table 1).

5.1.4. Monzonite

Zircon crystals in the monzonite (Sample 08LX66) are euhedral–subhedral, brown-yellow, have uniform sizes of ~100 μm, are mostly dark in CL images, and have wide oscillatory zoning in the cores (Fig. 2a). All 18 zircons analyzed are concordant and yield a mean $^{206}Pb/^{238}U$ age of 129.9 ± 0.8 Ma (2σ) (Fig. 2e and Table 1).

5.1.5. Syenodiorite

Zircon crystals in the syenodiorite (Sample 07SD74) are euhedral–subhedral, light maroon, and range from 200 to 600 μm in size, with length to width ratios of 1.5:1 to 2.5:1. They have wide oscillatory zoning in the core and narrow oscillatory zoning in the rim. Some zircons were lightly altered in their margin, as shown by the CL images (Fig. 2a). Nineteen of the 20 zircons analyzed yield a mean $^{206}Pb/^{238}U$ age of 131.7 ± 1.4 Ma (2σ) (Fig. 2f and Table 1). One analysis shows a $^{206}Pb/^{238}U$ age of 160 Ma, which is different from the others. There is no

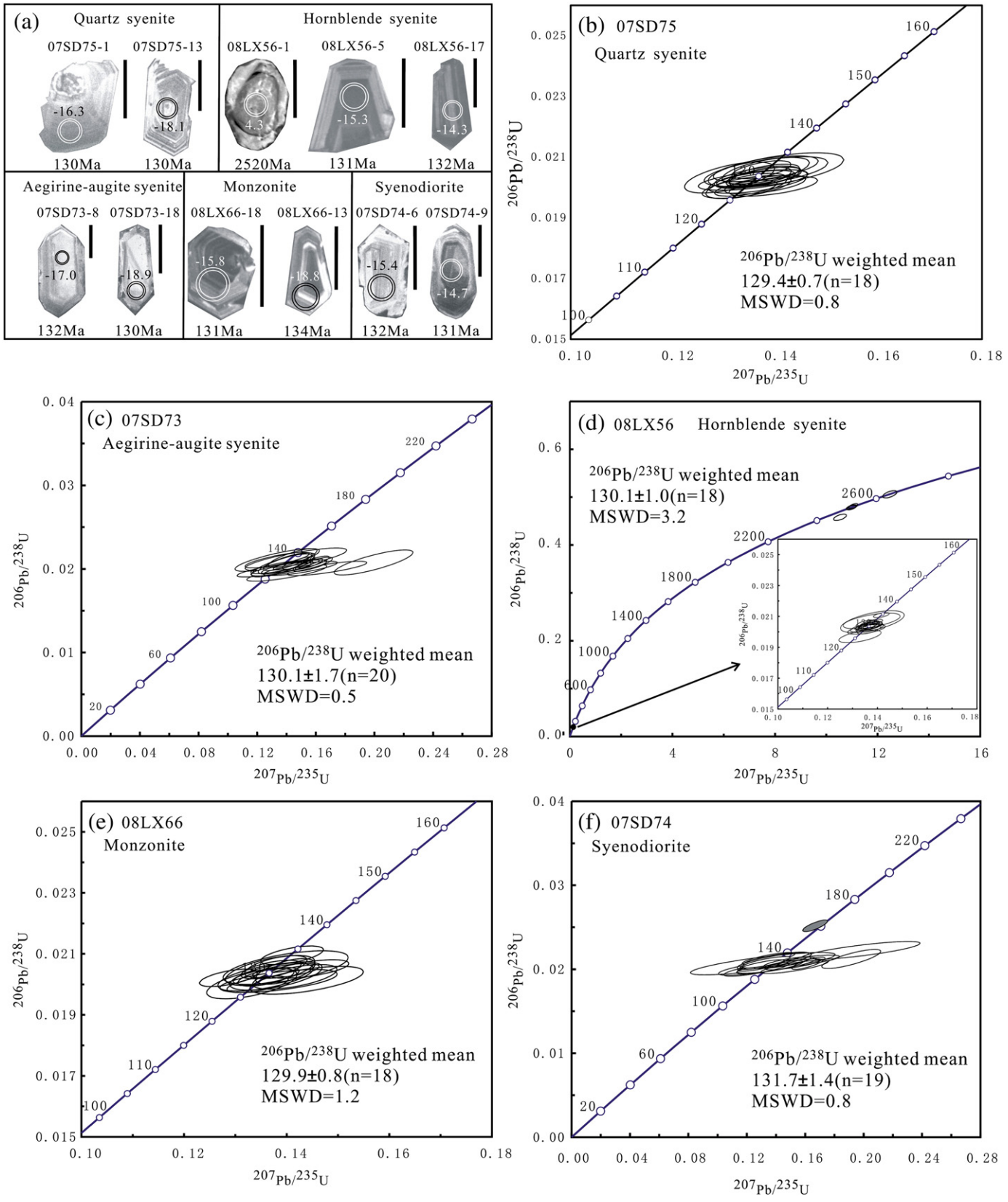

Fig. 2. Representative CL images of zircon grains (a) and LA–ICP-MS zircon U–Pb concordia diagrams of quartz syenite (b), porphyritic aegirine–augite syenite (c), porphyritic hornblende syenite (d), monzonite (e) and syenodiorite (f) from the Longbaoshan alkaline complex. Bigger circles represent locations of Hf isotopic analyses, smaller circles indicate spots of LA–ICP-MS U–Pb dating, the U–Pb age and $\varepsilon_{Hf}(t)$ values are given for each analytical spot, and the scale bar is 100 μm in (a).

known corresponding magmatic activity with an age of ~160 Ma in the Luxi Block, though this age is consistent with the ages of granites widely distributed in the Jiaodong Peninsula. This anomalous zircon may have come from granites collected from the Jiaodong Peninsula, which were crushed using the same machine as the Longbaoshan rocks on the same day.

Table 1
LA–ICP-MS U–Pb data of zircons for the Longbaoshan alkaline complex.

Spot	Th (ppm)	U (ppm)	Th/U	$^{207}Pb/^{206}Pb$	1σ	$^{207}Pb/^{235}U$	1σ	$^{206}Pb/^{238}U$	1σ	$^{206}Pb/^{238}U$ (Ma)	1σ
07SD75 (quartz syenite)											
1	733	108	0.68	0.0486	0.0014	0.1369	0.0040	0.0204	0.0002	129.9	1.3
2	314	703	0.45	0.0486	0.0018	0.1361	0.0051	0.0203	0.0002	129.5	1.1
3	305	493	0.62	0.0490	0.0021	0.1363	0.0055	0.0203	0.0002	129.8	1.5
4	209	519	0.40	0.0473	0.0022	0.1309	0.0058	0.0203	0.0003	129.7	2.1
5	824	686	1.20	0.0488	0.0019	0.1342	0.0052	0.0200	0.0003	128.0	1.7
6	5128	425	1.21	0.0487	0.0024	0.1380	0.0067	0.0206	0.0003	131.5	1.8
7	163	208	0.78	0.0499	0.0031	0.1380	0.0079	0.0205	0.0003	131.0	2.0
8	473	356	1.33	0.0496	0.0024	0.1364	0.0064	0.0202	0.0003	128.9	1.6
9	356	633	0.56	0.0492	0.0020	0.1379	0.0056	0.0206	0.0003	131.1	1.8
10	1297	818	1.58	0.0488	0.0015	0.1341	0.0040	0.0200	0.0002	127.5	1.1
11	407	684	0.59	0.0502	0.0019	0.1394	0.0057	0.0200	0.0002	127.9	1.4
12	557	833	0.67	0.0496	0.0018	0.1378	0.0052	0.0201	0.0002	128.2	1.3
13	1230	1730	0.71	0.0489	0.0017	0.1376	0.0049	0.0203	0.0002	129.8	1.3
14	466	781	0.60	0.0486	0.0026	0.1355	0.0071	0.0202	0.0002	129.2	1.4
15	273	227	1.21	0.0506	0.0033	0.1400	0.0087	0.0206	0.0004	131.2	2.4
16	621	913	0.68	0.0490	0.0017	0.1377	0.0045	0.0204	0.0002	130.3	1.4
17	283	609	0.46	0.0487	0.0021	0.1342	0.0057	0.0200	0.0002	127.8	1.6
18	1939	1561	1.24	0.0480	0.0013	0.1371	0.0038	0.0206	0.0002	131.3	1.2
07SD73 (aegirine–augite syenite)											
1	330	618	0.53	0.0519	0.0038	0.1463	0.0104	0.0204	0.0004	130.0	3.0
2	232	376	0.62	0.0553	0.0027	0.1581	0.0072	0.0208	0.0005	132.0	3.0
3	189	402	0.47	0.0492	0.0041	0.1438	0.0110	0.0212	0.0008	135.0	5.0
4	269	364	0.74	0.0461	0.0069	0.1332	0.0191	0.0210	0.0009	134.0	6.0
5	167	279	0.60	0.0503	0.0082	0.1461	0.0229	0.0211	0.0009	134.0	6.0
6	552	413	1.34	0.0480	0.0063	0.1311	0.0169	0.0198	0.0006	126.0	4.0
7	533	601	0.89	0.0548	0.0024	0.1550	0.0062	0.0205	0.0004	131.0	3.0
8	189	282	0.67	0.0698	0.0070	0.1992	0.0179	0.0207	0.0010	132.0	6.0
9	191	292	0.66	0.0461	0.0052	0.1333	0.0145	0.0210	0.0006	134.0	4.0
10	248	353	0.70	0.0542	0.0063	0.1492	0.0167	0.0200	0.0006	127.0	4.0
11	195	362	0.54	0.0522	0.0070	0.1399	0.0180	0.0194	0.0007	124.0	4.0
12	394	367	1.07	0.0492	0.0049	0.1397	0.0129	0.0206	0.0008	131.0	5.0
13	237	369	0.64	0.0558	0.0034	0.1575	0.0089	0.0205	0.0006	131.0	4.0
14	290	591	0.49	0.0521	0.0028	0.1481	0.0074	0.0206	0.0005	132.0	3.0
15	215	334	0.64	0.0488	0.0050	0.1356	0.0134	0.0201	0.0005	129.0	3.0
16	224	522	0.43	0.0506	0.0044	0.1402	0.0117	0.0201	0.0005	128.0	3.0
17	241	399	0.60	0.0512	0.0065	0.1413	0.0172	0.0200	0.0006	128.0	4.0
18	240	375	0.64	0.0486	0.0053	0.1361	0.0137	0.0203	0.0009	130.0	6.0
19	165	286	0.58	0.0490	0.0041	0.1404	0.0110	0.0208	0.0007	133.0	4.0
20	226	331	0.68	0.0608	0.0067	0.1675	0.0179	0.0200	0.0006	127.0	4.0
08LX56 (hornblende syenite)											
1	108	768	0.14	0.1661	0.0016	11.0535	0.1194	0.4813	0.0035	2532.7	15.0
2	19	60	0.32	0.1784	0.0023	12.4738	0.1840	0.5059	0.0050	2639.0	21.5
3	62	87	0.72	0.1664	0.0023	10.5342	0.1666	0.4579	0.0044	2430.1	19.5
4	58	84	0.69	0.1663	0.0019	10.9882	0.1189	0.4786	0.0029	2521.3	12.6
5	631	987	0.64	0.0483	0.0010	0.1366	0.0027	0.0205	0.0002	130.6	1.2
6	72	114	0.63	0.1659	0.0020	10.9713	0.1316	0.4784	0.0029	2520.1	12.5
7	568	886	0.64	0.0485	0.0012	0.1367	0.0036	0.0204	0.0002	130.0	1.1
8	1198	1458	0.82	0.0486	0.0011	0.1372	0.0031	0.0204	0.0001	130.5	0.9
9	980	1068	0.92	0.0486	0.0010	0.1366	0.0028	0.0203	0.0002	129.9	1.2
10	445	704	0.63	0.0421	0.0032	0.1380	0.0085	0.0207	0.0005	131.8	2.9
11	674	898	0.75	0.0488	0.0010	0.1363	0.0027	0.0203	0.0001	129.5	0.9
12	54	308	0.17	0.1662	0.0019	10.9845	0.1324	0.4787	0.0035	2521.7	15.1
13	468	930	0.50	0.0473	0.0011	0.1340	0.0032	0.0202	0.0002	129.2	1.0
14	2453	1432	1.71	0.0486	0.0008	0.1384	0.0025	0.0206	0.0001	131.6	0.8
15	297	230	1.29	0.0493	0.0023	0.1330	0.0056	0.0197	0.0003	125.8	1.7
16	5558	3644	1.52	0.0488	0.0007	0.1371	0.0019	0.0204	0.0002	130.5	1.2
17	796	2040	0.39	0.0477	0.0028	0.1377	0.0076	0.0207	0.0003	132.1	2.1
18	266	435	0.61	0.0491	0.0014	0.1369	0.0037	0.0203	0.0002	129.3	1.2
19	3765	2714	1.39	0.0490	0.0014	0.1371	0.0032	0.0204	0.0002	130.2	1.0
20	182	218	0.84	0.0489	0.0019	0.1356	0.0050	0.0202	0.0002	128.7	1.3
21	566	1431	0.40	0.0478	0.0010	0.1352	0.0025	0.0205	0.0002	131.0	1.0
22	4664	2779	1.68	0.0486	0.0007	0.1416	0.0021	0.0211	0.0001	134.5	0.7
23	346	335	1.03	0.0487	0.0013	0.1362	0.0035	0.0203	0.0002	129.7	1.0
24	2114	1597	1.32	0.0487	0.0009	0.1366	0.0032	0.0202	0.0002	128.8	1.3
08LX66 (monzonite)											
1	812	361	2.25	0.0464	0.0014	0.1287	0.0037	0.0202	0.0002	129.0	1.2
2	420	275	1.53	0.0498	0.0027	0.1384	0.0076	0.0201	0.0002	128.4	1.6
3	977	506	1.93	0.0482	0.0022	0.1332	0.0058	0.0200	0.0003	127.8	2.1
4	1470	491	2.99	0.0489	0.0013	0.1360	0.0036	0.0202	0.0002	129.1	1.2
5	1524	507	3.01	0.0486	0.0014	0.1343	0.0039	0.0200	0.0002	127.7	1.1
6	864	318	2.72	0.0519	0.0026	0.1439	0.0073	0.0201	0.0003	128.5	1.9

Table 1 *(continued)*

Spot	Th (ppm)	U (ppm)	Th/U	$^{207}Pb/^{206}Pb$	1σ	$^{207}Pb/^{235}U$	1σ	$^{206}Pb/^{238}U$	1σ	$^{206}Pb/^{238}U$ (Ma)	1σ
08LX66 (monzonite)											
7	997	396	2.52	0.0487	0.0015	0.1360	0.0042	0.0203	0.0002	129.4	1.2
8	492	364	1.35	0.0510	0.0019	0.1444	0.0051	0.0205	0.0002	130.8	1.3
9	812	332	2.45	0.0496	0.0015	0.1399	0.0043	0.0204	0.0002	130.4	1.0
10	374	204	1.83	0.0494	0.0031	0.1398	0.0080	0.0206	0.0004	131.1	2.3
11	770	406	1.90	0.0484	0.0013	0.1370	0.0039	0.0205	0.0002	130.7	1.3
12	790	320	2.47	0.0508	0.0020	0.1416	0.0054	0.0202	0.0003	129.2	1.7
13	2596	637	4.08	0.0488	0.0014	0.1410	0.0040	0.0210	0.0002	133.7	1.3
14	533	380	1.40	0.0489	0.0014	0.1379	0.0040	0.0206	0.0002	131.3	1.5
15	640	280	2.29	0.0490	0.0023	0.1359	0.0061	0.0202	0.0003	129.2	1.9
16	651	377	1.72	0.0490	0.0020	0.1379	0.0059	0.0203	0.0003	129.4	1.9
17	961	546	1.76	0.0497	0.0013	0.1397	0.0038	0.0204	0.0003	130.3	1.7
18	627	413	1.52	0.0486	0.0019	0.1368	0.0058	0.0205	0.0003	130.5	2.1
07SD74 (syenodiorite)											
1	230	298	0.77	0.0480	0.0060	0.1384	0.0169	0.0209	0.0007	133.0	4.0
2	461	508	0.91	0.0461	0.0043	0.1344	0.0120	0.0212	0.0005	135.0	3.0
3	455	501	0.91	0.0465	0.0039	0.1330	0.0108	0.0208	0.0005	132.0	3.0
4	755	1146	0.66	0.0478	0.0052	0.1395	0.0147	0.0212	0.0005	135.0	3.0
5	384	570	0.67	0.0515	0.0039	0.1474	0.0108	0.0208	0.0004	132.0	3.0
6	365	360	1.02	0.0570	0.0029	0.1619	0.0075	0.0206	0.0005	132.0	3.0
7	1808	1789	1.01	0.0481	0.0018	0.1666	0.0057	0.0251	0.0005	160.0	3.0
8	120	201	0.60	0.0657	0.0051	0.1914	0.0134	0.0211	0.0007	135.0	5.0
9	295	443	0.67	0.0536	0.0047	0.1514	0.0128	0.0205	0.0004	131.0	3.0
10	371	514	0.72	0.0461	0.0039	0.1292	0.0106	0.0204	0.0005	130.0	3.0
11	176	272	0.65	0.0461	0.0040	0.1311	0.0108	0.0206	0.0005	132.0	3.0
12	504	320	1.58	0.0535	0.0071	0.1532	0.0199	0.0208	0.0006	133.0	3.0
13	120	185	0.65	0.0498	0.0066	0.1401	0.0179	0.0204	0.0006	130.0	4.0
14	149	292	0.51	0.0548	0.0057	0.1524	0.0154	0.0202	0.0005	129.0	3.0
15	311	219	1.42	0.0470	0.0075	0.1309	0.0204	0.0202	0.0007	129.0	4.0
16	1363	965	1.41	0.0504	0.0044	0.1430	0.0121	0.0206	0.0004	131.0	2.0
17	222	87	2.54	0.0461	0.0118	0.1307	0.0329	0.0206	0.0009	131.0	6.0
18	1579	1638	0.96	0.0649	0.0091	0.1980	0.0270	0.0221	0.0007	141.0	4.0
19	270	236	1.14	0.0487	0.0056	0.1353	0.0151	0.0202	0.0005	129.0	3.0
20	322	255	1.26	0.0461	0.0056	0.1264	0.0149	0.0199	0.0006	127.0	3.0

5.2. Major and trace elements

Major and trace element analyses are presented in Table 2. The major oxides of the quartz syenite, the aegirine–augite syenite, and the hornblende syenite are similar to each other. They are all high in SiO_2 (63.8–70.7 wt.%), Al_2O_3 (16.3–18.2 wt.%), and $Na_2O + K_2O$ (10.5–11.8 wt.%) and low in CaO (0.20–1.85 wt.%), TFe_2O_3 (1.24–3.28 wt.%), MgO (0.09–1.29 wt.%), and TiO_2 (0.14–0.44 wt.%). The monzonite and syenodiorite have lower SiO_2 (58.5–63.4 wt.%), CaO (1.14–3.39 wt.%), and TFe_2O_3 (2.65–4.28 wt.%), but Al_2O_3 (16.1–19.0 wt.%), TiO_2 (0.26–0.37 wt.%), and $Na_2O + K_2O$ (9.5–11.2 wt.%) are similar to others. The syenodiorite have the highest MgO (3.33 wt.%). The Mg# varies greatly from 6.4 to 63.5, and the monzonite and the syenodiorite have relatively high Mg# (Table 2). All samples except for the syenodiorite fall into the fields of syenite and quartz syenite in the R1 vs. R2 diagram (Fig. 3a). They are metaluminous to peraluminous (Fig. 3b).

All samples have similar Chondrite-normalized REE patterns (Fig. 4). They are characterized by LREE enrichment ($\sum$LREE = 207–1107 ppm), strong fractionation between LREE and HREE ($(La/Yb)_N = 33–130$), slight fractionation of HREE ($(Gd/Yb)_N = 2.87–6.27$), and small negative Eu anomalies ($\delta Eu = 0.66–0.86$). On the primitive mantle-normalized spidergrams (Fig. 4), the samples are enriched in LILE such as Ba (1536–5127 ppm), Th, U and Pb and depleted in HFSE such as Nb, Ta, Zr, Hf, P and Ti. Samples are also enriched in Sr (567–2891 ppm), except for three hornblende syenite samples (08LX47, 08LX55 and 08LX56).

5.3. Sr–Nd–Pb isotopes

Sr, Nd and Pb isotopic compositions of the Longbaoshan alkaline complex are presented in Table 3 and shown in Fig. 5. The quartz syenite and syenodiorite have uniform initial $^{87}Sr/^{86}Sr$ ratios (0.7077–0.7080) and $\varepsilon_{Nd}(t)$ (−12.7 to −11.8), whereas the aegirine–augite syenite, hornblende syenite, and monzonite have higher initial $^{87}Sr/^{86}Sr$ ratios (0.7080–0.7094) and lower $\varepsilon_{Nd}(t)$ (−15.8 to −12.3). All samples have similar Pb isotopic compositions ($(^{206}Pb/^{204}Pb)i = 17.24–17.95$, $(^{207}Pb/^{204}Pb)i = 15.48–15.59$, $(^{208}Pb/^{204}Pb)i = 37.36–38.00$), which plot above the North Hemisphere Reference Line (NHRL) in the $^{206}Pb/^{204}Pb$ vs. $^{208}Pb/^{204}Pb$ diagram (Fig. 6).

5.4. Zircon Hf isotope data

In situ Hf isotopic analyses of zircons from the Longbaoshan complex are listed in Table 4 and shown in Fig. 7. There are no obvious differences of $\varepsilon_{Hf}(t)$ values between the rocks. Eighteen analyses obtained from 18 grains for the quartz syenite (07SD75) yield $\varepsilon_{Hf}(t)$ values between −19.2 and −14.0 with average value of −16.1. Twenty analyses obtained from 20 grains for the aegirine–augite syenite (07SD73) yield $\varepsilon_{Hf}(t)$ values between −18.9 and −15.7 with an average value of −17.0. Zircons from the hornblende syenite (08LX56) yield $\varepsilon_{Hf}(t)$ values between −18.3 and −13.5 with an average value of −15.7, except for the inherited zircons which show positive $\varepsilon_{Hf}(t)$ values ranging from 0.2 to 6.2. The $\varepsilon_{Hf}(t)$ values of zircons from the monzonite from eighteen analyses vary from −18.9 to −14.7, with an average value of −16.5. Twenty analyses of zircons from the syenodiorite (07SD74) yield $\varepsilon_{Hf}(t)$ values between −16.5 and −12.8 with the highest average value of −14.8.

6. Discussion

6.1. Intrusive age and inherited zircons

From the quartz syenite to the syenodiorite, the LA–ICP-MS zircon U–Pb ages vary little from 129.4 to 131.7 Ma, which are similar to the Rb–Sr isochron age (129.3 ± 4.5) derived from the Longbaoshan complex by Zhang et al. (2005a). However, the zircon U–Pb isotopic

Table 2
Major oxides (wt.%) and trace elements (ppm) for the Longbaoshan alkaline complex.

Sample no.	07DS71	07SD75	07SD76	07SD77	07SD67	07SD72	07SD73	08LX60	08LX65	08LX52	08LX53	08LX54	S08LX55	08LX56	08LX57	08LX47	08LX50	08LX59	08LX61	08LX66	07SD74	GSR1	GSR1
Rock-type	Quartz syenite				Aegirine–augite syenite					Hornblende syenite						Monzonite					Syenodiorite	Refer.	
SiO_2	69.7	70.7	70	69.6	67	66.9	67.7	65.4	64.2	66.4	66.9	63.8	64.8	64	65	60	58.5	59.4	61.9	63.4	61.5	73.1	72.8
TiO_2	0.2	0.15	0.14	0.16	0.28	0.22	0.24	0.44	0.31	0.22	0.22	0.35	0.28	0.21	0.27	0.37	0.35	0.35	0.47	0.26	0.45	0.28	0.28
Al_2O_3	16.5	16.3	16.3	16.7	17.4	17.8	17	16.9	18.4	17.1	17.4	18.3	18.3	17.1	18.1	18.3	17.8	17.3	17.2	19	16.1	13.4	13.4
TFe_2O_3	1.24	1.58	1.43	1.49	2.59	2.04	2.07	1.47	2.56	2.27	2.3	3.28	2.74	2.18	1.95	4.28	3.92	3.09	3.77	2.65	4.11	2.13	2.14
MnO	0.03	0.01	0.05	0.02	0.05	0.06	0.04	0.03	0.03	0.06	0.02	0.07	0.04	0.07	0.05	0.11	0.1	0.07	0.05	0.04	0.07	0.06	0.06
MgO	0.1	0.11	0.15	0.15	0.09	0.14	0.47	1.29	0.29	0.22	0.2	0.3	0.24	0.6	0.36	0.27	0.78	1.1	1.64	0.4	3.33	0.41	0.42
CaO	0.28	0.71	0.71	0.56	0.82	0.62	1.23	1.85	1.06	0.36	0.44	0.5	0.2	1.62	0.33	2.72	3.39	2.87	2.16	1.4	3.64	1.54	1.55
Na_2O	5.63	6.34	6.66	6.33	5.37	6.96	6.42	4.41	6.66	6.51	6.35	6.22	6.05	6.09	5.32	5.29	5.43	5.02	5.84	6.68	5.47	3.11	3.13
K_2O	5.74	4.18	4.19	4.19	5.77	4.8	4.36	6.67	4.56	4.9	4.83	4.48	5.14	5.13	5.31	4.27	4.09	5.15	4.5	4.51	4.28	5.02	5.01
P_2O_5	0.05	0.06	0.04	0.04	0.18	0.06	0.13	0.24	0.19	0.11	0.12	0.23	0.14	0.11	0.15	0.34	0.32	0.23	0.41	0.2	0.42	0.09	0.09
LOI	0.63	0.38	0.6	0.47	0.53	0.53	0.37	0.84	0.98	1.26	1.06	1.94	1.56	2.96	2.44	4.12	4.65	4.8	1.6	0.96	0.73	0.69	0.69
Total	100.3	100.7	100.5	99.8	100.1	100.3	100	99.6	99.3	99.3	99.8	99.5	99.5	100	99.3	100	99.3	99.4	99.5	99.5	100	99.8	99.6
Mg#	11.9	10.8	15.2	14.8	6.4	10.9	31	63.5	18.3	16.1	14.7	15.3	14.8	35.3	26.8	11.1	28.3	41.4	46.3	23	61.6		
Cr	22.7	27.9	45.8	21.8	34.6	18.9	31.3	90.9	60	60.8	52.1	51.4	46.7	88.5	54.5	39.8	36.3	51.6	98.4	49.8	95.8	2.79	5
Co	0.69	1.65	1.37	1.6	2.2	2.1	3	3.58	8.76	4.37	3.33	6.41	3.99	3.3	4.24	7.02	5.3	5.69	9.07	4.43	14.6	3.4	3.4
Ni	2.36	1.36	1.41	4.23	3.71	1.83	4.18	13.5	7.27	7.66	6.66	10.9	6.05	8.08	8.09	4.97	3.44	8.3	16.3	2.66	67.1	3.1	2.3
Rb	91.2	45	47	53.1	103	75.9	68.4	131	69	97.2	91.7	68	88.8	86.4	96.5	74.8	81.5	92.4	86.3	59.6	76.2	481	466
Sr	654	1316	1146	1361	1491	1924	2031	1540	2700	856	1289	672	379	223	569	206	971	1036	1357	2891	1747	112	106
Cs	0.4	0.17	0.2	0.19	1.56	0.34	1.09	1.08	1.26	3.22	1.11	0.55	1.68	1.47	1.18	1.93	2.35	3.17	3.01	0.64	3.22	39.3	38.4
Ba	1536	2442	2485	2199	3063	3720	3037	3269	470	1938	2135	4547	3870	2713	4398	2132	3984	4935	2854	5127	2581	337	343
La	101	65.9	66.5	65.1	152	128	109	210	239	138	113	155	96.8	88.4	115	329	332	214	262	208	122	53.6	54
Ce	180	99.7	119	75.2	266	249	222	333	367	254	238	335	224	164	198	504	532	354	430	341	212	108	108
Pr	16.7	13.1	13	13.3	29.2	26.4	22.4	32.7	36.3	25.5	22.2	30.8	19.3	18.4	22.8	50.1	52.3	37.8	42.5	29.7	26.1	13.3	12.7
Nd	56.1	44.7	44.7	45.6	94.6	92.1	76.7	104.5	114.1	88.2	77	102	60.2	65.9	74.6	167	166	123	144	94.6	85.9	48.9	47
Sm	7.6	6.26	6.82	6.69	13	12.6	10.6	13.4	14.2	11.9	10.7	15.2	9.17	9.74	11.3	20.6	19.6	16.8	19.1	11.9	13.5	10.1	9.7
Eu	1.57	1.37	1.57	1.57	2.97	2.76	2.3	2.91	3.43	2.6	2.48	3.5	2.29	2.17	2.48	4.42	4.26	3.85	4.05	2.93	3.05	0.85	0.85
Gd	6.63	4.27	5.09	4.9	10.6	8.33	7.25	10.3	10.4	8.92	7.95	11.4	7.41	7.05	7.67	16.47	14.91	12.3	14.21	8.16	9.99	9.36	9.3
Tb	0.72	0.5	0.53	0.5	0.96	0.89	0.78	1	1.03	0.93	0.85	1.22	0.87	0.78	0.86	1.43	1.3	1.2	1.39	0.75	0.94	1.65	1.65
Dy	3.6	2.38	2.53	2.33	4.05	3.93	3.58	4.07	4.43	4.02	3.9	5.07	4.04	3.54	3.91	6.09	5.12	4.68	5.65	2.95	3.9	10.7	10.2
Ho	0.68	0.44	0.48	0.44	0.72	0.66	0.63	0.71	0.72	0.7	0.69	0.88	0.73	0.63	0.7	1.04	0.84	0.77	0.96	0.49	0.65	2.25	2.05
Er	1.92	1.21	1.29	1.14	1.99	1.74	1.63	1.92	1.84	1.84	1.81	2.28	1.94	1.72	1.83	2.68	2.23	1.9	2.35	1.26	1.68	6.97	6.5
Tm	0.29	0.18	0.2	0.18	0.28	0.25	0.25	0.28	0.26	0.27	0.27	0.31	0.28	0.25	0.27	0.35	0.31	0.27	0.33	0.17	0.23	1.12	1.06
Yb	1.86	1.19	1.34	1.18	1.81	1.66	1.59	1.75	1.67	1.83	1.73	1.98	1.79	1.55	1.7	2.19	1.92	1.68	2	1.07	1.43	7.81	7.4
Lu	0.28	0.19	0.21	0.18	0.26	0.25	0.24	0.26	0.25	0.28	0.26	0.3	0.27	0.24	0.27	0.33	0.29	0.25	0.32	0.17	0.21	1.25	1.15
Y	20.5	14.3	14.1	12.2	20.4	18.6	17.8	21	21.5	20.9	20.4	23.8	20.5	19.7	19.8	28.5	23.4	22.1	27.1	14.1	18.8	63.6	62
Zr	329	223	215	185	322	329	262	438	344	358	390	422	398	366	409	437	437	417	425	364	246	170	167
Hf	8.45	5.72	6.14	4.74	8.58	8.25	6.46	10.34	8.3	9.02	9.53	9.4	8.75	8.73	9.23	9.43	9.63	8.63	9.6	7.97	6.04	6.5	6.3
Nb	40.9	24.7	33	21.4	26	23.3	22.6	24.5	19.3	38.7	38.7	21.6	22.6	24	23.6	19.1	18.9	19.5	26.7	11	18.2	41.7	40
Ta	2.43	1.07	1.58	1.09	1.43	1.2	1.14	1.42	1.04	1.99	2	1.25	1.31	1.21	1.28	0.92	0.93	1.1	1.31	0.63	0.85	7.4	7.2
Th	58.5	27.2	34.9	19	48.1	55.1	37.5	49.2	39.7	47.9	48.5	39.6	38.7	37.9	40.4	41.7	43.5	40.2	50.1	37	23.8	55.8	54
U	5.87	3.2	6.87	2.89	6.6	4.21	4.09	4.6	4.71	13.3	11	5.42	5.18	7.2	9.73	3.87	6.49	6.24	6.12	2.85	3.77	18.9	18.8
Pb	31.8	84.6	29.8	26.8	39.9	92.5	31.1	37.1	22.7	45.8	61.4	34.5	38.3	36.2	28.9	25.9	21.4	37.8	23.5	31.1	20.7	32.8	31
δEu	0.66	0.77	0.78	0.8	0.75	0.77	0.76	0.73	0.83	0.74	0.79	0.78	0.83	0.76	0.77	0.71	0.73	0.78	0.72	0.86	0.77		

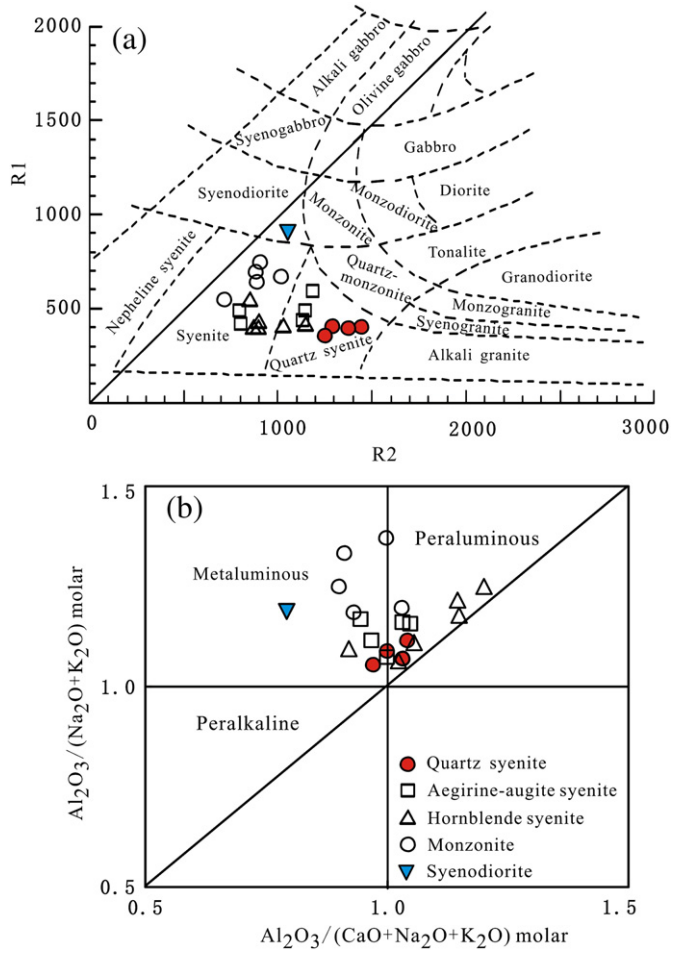

Fig. 3. Plots of (a) R1 vs. R2 [R1 = 4Si-11(Na + K)-2(Fe + Ti),R2 = 6Ca + 2 Mg + Al] and (b) A/NK [molar ratio $Al_2O_3/(Na_2O+K_2O)$] vs. A/CNK [molar ratio $Al_2O_3/(CaO+Na_2O+K_2O)$]. Panel (a) is from De la Roche et al. (1980).

system provides the most reliable age for crystalline rocks because it has the highest closure temperature and strong resistance to overprinting geological processes, whereas the Rb–Sr isochron age can be less reliable due to the small variations in $^{87}Rb/^{86}Sr$ and $^{87}Sr/^{86}Sr$ ratios (Zhang et al., 2005a). Thus, we consider the 129.4–131.7 Ma ages as representative of the crystallization timing of the whole Longbaoshan alkaline intrusive complex.

The ages of 2512–2639 Ma, derived from inherited zircon cores, are similar to the ages of the basement rocks (Wang et al., 2009) widely distributed in the Luxi Block.

6.2. Petrogenesis

6.2.1. Mantle source

According to the similar/same intrusive ages, Sr–Nd–Pb–Hf isotopic compositions, $Na_2O + K_2O$ contents (9.5–11.8 wt.%), normalized REE patterns and trace element spidergrams and the close spatial relationship, we regard that quartz syenite, aegirine–augite syenite, hornblende syenite, monzonite and syenodiorite are the members of one intrusion (Longbaoshan alkaline complex), although they are diverse in certain compositions. All the Sr, Nd and Pb isotopic compositions of the Longbaoshan complex are different from the upper and lower crust of the NCC and the late Archean basement rocks in the Luxi Block (Jahn et al., 1988, 1999), but similar to the nearby Fangcheng basalts and Yinan gabbros (Figs. 5 and 6), which were derived from EM2 source (Xu et al., 2004b; Zhang et al., 2002). In addition, the Hf isotopic compositions of the Longbaoshan complex fall above the 2.5 Ga continental crust evolutional line (Fig. 7a), and are consistent with the early Cretaceous enriched lithospheric mantle (EM2) beneath the Luxi Block (Fig. 7b). Thus, it is reasonable to deduce that the Longbaoshan complex mainly originated from EM2-type lithospheric mantle.

The Longbaoshan complex is characterized by strong fractionation between LREE and HREE, enrichment of LILEs and depletion of HFSEs (Fig. 4), which are the common features of the early Cretaceous mafic intrusions and volcanics in the southeastern NCC (Zhang and Sun, 2002; Zhang et al., 2005b). These features are similar to some arc volcanics (e.g., sanukitoids and adakites) that are commonly associated with slab subduction (Furukawa and Tatsumi, 1999; Kamei et al., 2004; Yogodzinski et al., 1995). The high La/Nb and Ba/Nb ratios of the Longbaoshan complex also fall into the field of the arc volcanics (Fig. 8), implicating that the mantle source of the Longbaoshan complex was similar to the mantle wedge in the subduction zone. The enrichment of this mantle source, therefore, may be attributed to subduction-related metasomatism, as indicated by the high $(Hf/Sm)_N$ and low $(Ta/Th)_N$ ratios of the Longbaoshan complex and the Jinan gabbros in the Luxi Block (Fig. 9a). This has strongly proven the high Nb/Ta ratios of the Longbaoshan complex as well as the Mesozoic basalts in the eastern NCC. The Nb/Ta ratios of the Longbaoshan complex vary from 16.7 to 23.2, with an average value of 19.2, which is higher than continental crust (12–13, Barth et al., 2000), MORB (16.7 ± 1.8, Kamber and Collerson, 2000), PM (17.5 ± 2.0, Green, 1995; Sun and McDonough, 1989), and Cenozoic basalts (15.1 ± 0.7, Liu and Gao, 2007; Liu et al., 2008b) in the eastern NCC, but similar to Mesozoic basalts in the eastern NCC (19.9 ± 1.0, Liu and Gao, 2007) (Fig. 9b). In the most mantle magmatic processes, Nb and Ta were thought to behave as identical twins due to their similar cationic radii and valence state (Liu et al., 2008b; Taylor and McLennan, 1985). However, experiments have demonstrated that Nb and Ta fractionate when Ti-rich minerals, such as rutile, ilmenite and sphene are involved in melting or crystal fractionation (Green, 1995; Green and Pearson, 1987). Rutile especially partition Nb and Ta ($D_{Nb,Ta}^{rutile/melt} > 1$) and effectively fractionates Nb from Ta ($D_{Nb}/D_{Ta}^{rutile/melt} < 1$) (Bromiley and Reffern, 2008; Foley et al., 2000; Klemme et al., 2005; Liang et al., 2009; Schmidt et al., 2004; Xiong et al., 2005), such that melts in equilibrium with rutile will be characterized by high Nb/Ta ratios (Liu et al., 2008b). Moreover, both natural samples and experimental products indicate that rutile is a common mineral phase in eclogite (Jacob, 2004; Rapp et al., 1999; Rudnick et al., 2000; Xiong et al., 2005; Xu et al., 2006) and important Ti-bearing phase responsible for the distribution and concentration of Nb and Ta in the subduction setting (Green, 1995; Liang et al., 2009). Therefore, combined with the high $(^{87}Sr/^{86}Sr)_i$ ratios and low $\varepsilon_{Nd}(t)$ values of the mafic rocks (Xu et al., 2004b; Zhang and Sun, 2002; Zhang et al., 2002), it is regarded that the early Cretaceous lithospheric mantle beneath the Luxi Block had been metasomatized by continental crust-derived melts which were in equilibrium with rutile-bearing eclogite in settings similar to subduction zone. Based on Sr–Nd studies on basalts and gabrros, 20–30% crustal materials were assimilated in the lithospheric mantle (Xu et al., 2004b; Zhang et al., 2002), giving rise to the formation of the EM2-type lithospheric mantle.

The subducted Yangtze continental crust is considered as the perfect candidate responsible for the enrichment of the lithospheric mantle, which is advocated by the regular variation of Sr–Nd isotopic compositions from the northwestern to southeastern Luxi Block and the proximity of the Luxi Block to the suture zone between the NCC and the YC. Reactions between lithospheric peridotite and silica-rich melt originating from the subducted Yangtze crust significantly changed the composition of the lithospheric mantle (Zhang et al., 2005b). Geochemistry of Mesozoic volcanic rocks reveals that the area influenced extends from the Dabie UHP metamorphic belt north about

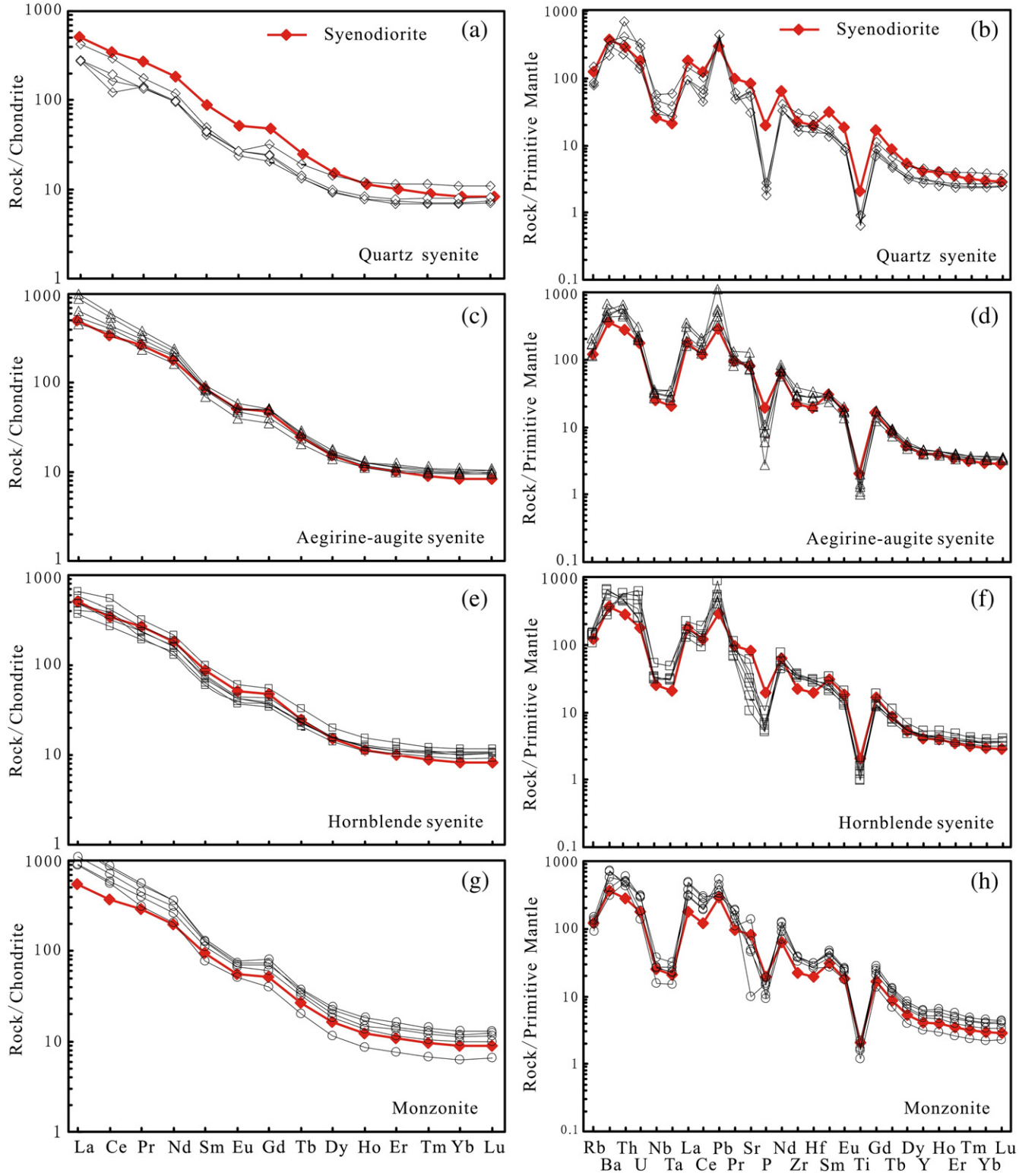

Fig. 4. Chondrite-normalized REE patterns and Primitive Mantle (PM) normalized trace element diagrams for quartz syenite (a and b), aegirine–augite syenite (c and d), hornblende syenite (e and f), monzonite (g and h) and syenodiorite. Syenodiorite is shown in each subgraph for comparison. Chondrite and PM values are from Sun and McDonough (1989).

450 km, reaching the Tai'an–Laiwu region of the Luxi Block (Zhang and Sun, 2002; Zhang et al, 2005b).

However, delamination was also proposed as an alternative solution to the genesis of the EM. In the delamination model, the EM was produced by reaction between mantle peridotite and silica-rich melt derived from the delaminated lower crust (Gao et al., 2008, 2009; Liu et al., 2008a; Qiu et al., 2005; Xu et al., 2006, 2008; Yang, 2007; Yang et al., 2005a, 2008). It was proposed that inherited zircons with late Archean ages and peridotite xenoliths with crustal Sr and Nd isotopic compositions in the high-Mg diorites (Xu et al., 2008; Yang, 2007) were persuasive evidence of the involvement of foundered lower crust. Enrichment of LILEs, depletion of HFSEs and HREE, and high (La/Yb)n and Sr/Y ratios in the high-Mg diorites were considered as adakitic features, which should be produced by melting of the

Table 3
Sr–Nd–Pb isotopic compositions for the Longbaoshan alkaline complex.

Sample	Age (Ma)	Rb (ppm)	Sr (ppm)	$^{87}Rb/^{86}Sr$	$^{87}Sr/^{86}Sr$	±2σ	$(^{87}Sr/^{86}Sr)_i$	Sm (ppm)	Nd (ppm)	$^{147}Sm/^{144}Nd$	$^{143}Nd/^{144}Nd$	±2σ	$\varepsilon_{Nd}(t)$	$^{206}Pb/^{204}Pb$	$^{207}Pb/^{204}Pb$	$^{208}Pb/^{204}Pb$
Quartz syenite																
07SD075	130	45.0	1441.2	0.0903	0.707828	11	0.707661	6.2	43.0	0.0867	0.511911	12	−12.4	17.530	15.495	37.867
07SD076	130	47.7	1265.8	0.1090	0.707969	8	0.707768	6.1	40.8	0.0899	0.511940	11	−11.8	17.524	15.315	37.922
07SD077	130	53.4	1481.7	0.1043	0.707722	9	0.707529	6.1	42.9	0.0867	0.511901	10	−12.6	17.281	15.367	37.682
Aegirine–augite syenite																
07SD067	130	109.1	1856.9	0.1701	0.709081	11	0.708767	12.8	96.1	0.0802	0.511798	14	−14.5	17.980	15.375	38.524
07SD072	130	76.9	2148.1	0.1037	0.709118	10	0.708927	12.1	89.6	0.0819	0.511834	11	−13.8	17.515	15.468	38.081
07SD073	130	68.7	2245.1	0.0885	0.708347	8	0.708184	10.0	72.0	0.0837	0.511811	10	−14.3	17.325	15.297	37.876
Hornblende syenite																
08LX052	130	101.5	863.4	0.3404	0.708601	14	0.707973	11.6	82.3	0.0851	0.511914	12	−12.3	17.342	15.349	37.984
08LX055	130	87.4	363.5	0.6963	0.710613	10	0.709327	8.6	56.4	0.0926	0.511811	15	−14.4	17.448	15.367	38.082
Monzonite																
08LX047	130	83.2	205.8	1.1706	0.711585	12	0.709422	20.7	174.5	0.0719	0.511723	15	−15.8	17.316	15.235	38.285
08LX059	130	95.0	1035.3	0.2655	0.709669	10	0.709178	15.8	115.8	0.0825	0.511794	13	−14.6	17.374	15.358	38.095
08LX066	130	63.4	2987.8	0.0614	0.708544	9	0.708431	11.1	95.4	0.0705	0.511801	12	−14.2	17.261	15.323	37.985
Syenodiorite																
07SD074	131	80.1	1925.1	0.1205	0.708214	15	0.707989	13.2	90.1	0.0883	0.511893	12	−12.7	17.379	15.333	37.942

Chondrite Uniform Reservoir (CHUR) values ($^{87}Rb/^{86}Sr=0.0847$, $^{87}Sr/^{86}Sr=0.7045$, $^{147}Sm/^{144}Nd=0.1967$, $^{143}Nd/^{144}Nd=0.512638$) are used for the calculation. $\lambda_{Rb}=1.42\times10^{-11}$ year^{-1}, $\lambda_{Sm}=6.54\times10^{-12}$ year^{-1} (Lugmair and Harti, 1978). $\lambda_{U238}=1.55125\times10^{-10}$ year^{-1}, $\lambda_{U235}=9.8485\times10^{-10}$ year^{-1}, $\lambda_{Th232}=4.9475\times10^{-11}$ year^{-1} (Steiger and Jäger, 1977).

foundered and eclogitized lower crust. However, the above evidence is inadequate to prove the existence of delamination in the Luxi Block. The inherited zircons in high-Mg diorites may come from crustal contamination or mixing. The peridotite xenoliths with crustal Sr and Nd isotopic compositions can also be explained by metasomatism of subducted crust (Chen and Zhou, 2004). In addition, the relatively high HREE contents and insignificant fractionation between HREEs in these high-Mg diorites indicate that abundant hornblende may have been present in the melting source of the crustal end-member (Wu et al., 2003). However, delamination would not have occurred if large amounts of hornblende still existed in the thickened lower crust

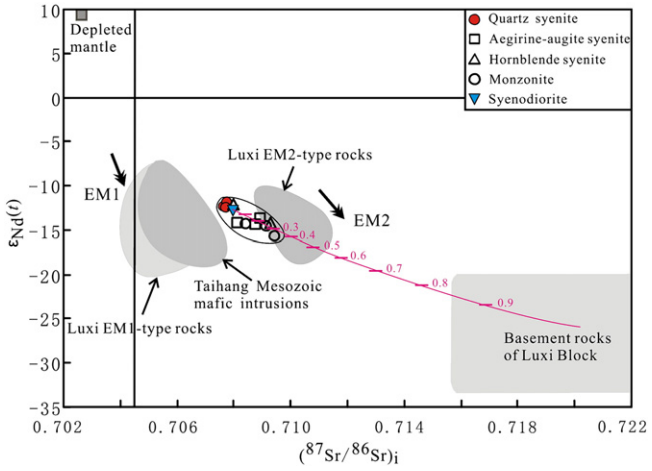

Fig. 5. Initial $^{87}Sr/^{86}Sr$ versus $\varepsilon_{Nd}(t)$ diagram for the Longbaoshan alkaline complex. Isotopic data for Mesozoic mafic intrusions from the Taihang Mountains (Chen and Zhai, 2003; Chen et al., 2003; Wang et al., 2006; Zhang et al., 2004) are shown for comparison. The EM1-type rocks in Luxi Block are from Guo et al. (2001), Yan et al. (2001), Xu et al. (2004a), Yang et al. (2005a), Yang (2007) and Li et al. (2007). The EM2-type rocks in Luxi Block are from Zhang et al. (2002), Xu et al. (2004b), Ying et al. (2004) and Yang (2007). The fields for basement rocks of Luxi Block are from Jahn et al. (1988). DM, EM1 and EM2 are from Zindler and Hart (1986). All $(^{87}Sr/^{86}Sr)_i$ and $\varepsilon_{Nd}(t)$ values are recalculated to 130 Ma. The mixing modelling parameters are Sr = 591 ppm, $^{87}Sr/^{86}Sr=0.720$, Nd = 42 ppm, $\varepsilon_{Nd}=-26$ for basement rocks of Luxi Block and Sr = 1925 ppm, $^{87}Sr/^{86}Sr=0.708$, Nd = 90 ppm, $\varepsilon_{Nd}=-13$ for enriched lithospheric mantle (represented by syenodiorite).

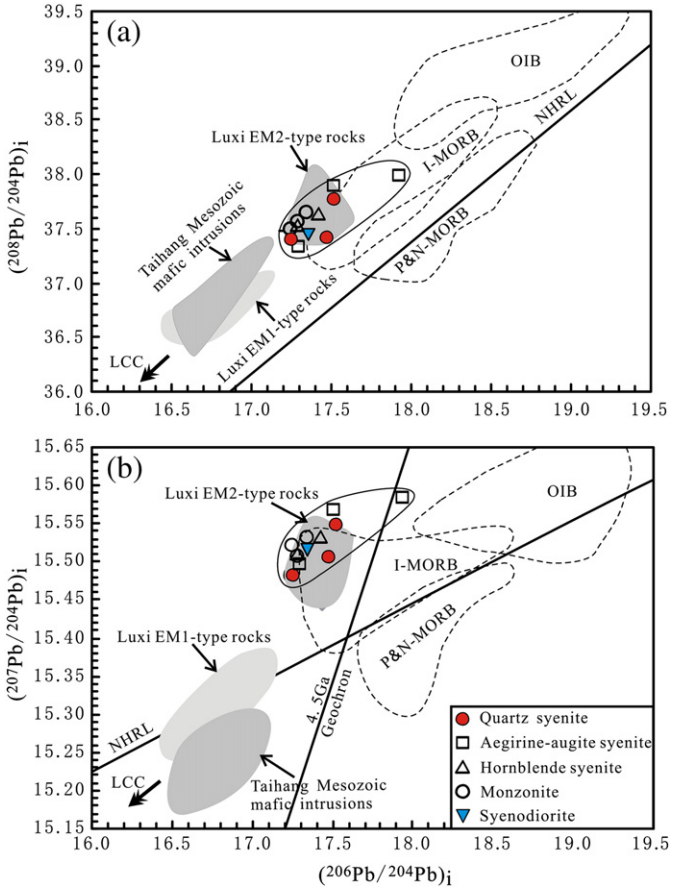

Fig. 6. $^{206}Pb/^{204}Pb$ vs. $^{208}Pb/^{204}Pb$(a) and $^{206}Pb/^{204}Pb$ vs. $^{207}Pb/^{204}Pb$(b) diagrams for the Longbaoshan alkaline complex. Isotopic data for Mesozoic mafic intrusions from the Taihang Mountains (Chen and Zhai, 2003; Wang et al., 2006; Zhang et al., 2004) are shown for comparison. The EM1-type rocks in Luxi Block are defined by the Jinan and Zouping gabbros (Li et al., 2007; Yang, 2007). The EM2-type rocks in Luxi Block are defined by the Fangcheng basalts (Zhang et al., 2002) and Yinan gabbros (Xu et al., 2004b). The fields for I-MORB (Indian MORB), P&N-MORB (Pacific and North Atlantic MORB), OIB, NHRL and 4.55 Ga geochron are from Hart (1984), Barry and Kent (1998) and Zou et al. (2000).

Table 4
Zircon Hf isotopic compositions for the Longbaoshan alkaline complex.

Spot no.	Age (Ma)	$^{176}Yb/^{177}Hf$	$^{176}Lu/^{177}Hf$	$^{176}Hf/^{177}Hf$	2σ	$\varepsilon_{Hf}(0)$	$\varepsilon_{Hf}(t)$	T_{DM1} (Ma)	T_{DM2} (Ma)	$f_{Lu/Hf}$
07SD75 (quartz syenite)										
1	130	0.005472	0.000182	0.282230	0.000022	−19.2	−16.3	1412	2223	−0.99
2	129	0.044490	0.001566	0.282196	0.000024	−20.4	−17.7	1512	2306	−0.95
3	130	0.024061	0.000766	0.282263	0.000020	−18.0	−15.2	1388	2153	−0.98
4	130	0.038434	0.001334	0.282254	0.000024	−18.3	−15.6	1421	2176	−0.96
5	128	0.028739	0.000865	0.282271	0.000020	−17.7	−15.0	1381	2138	−0.97
6	132	0.020078	0.000624	0.282241	0.000028	−18.8	−16.0	1414	2202	−0.98
7	131	0.016376	0.000532	0.282278	0.000022	−17.5	−14.7	1359	2118	−0.98
8	129	0.017803	0.000560	0.282168	0.000024	−21.4	−18.6	1511	2365	−0.98
9	131	0.024689	0.000809	0.282273	0.000023	−17.7	−14.9	1376	2131	−0.98
10	127	0.074971	0.002321	0.282249	0.000030	−18.5	−15.9	1467	2193	−0.93
11	128	0.037692	0.001246	0.282247	0.000022	−18.6	−15.9	1428	2192	−0.96
12	128	0.052609	0.001766	0.282153	0.000024	−21.9	−19.2	1582	2405	−0.95
13	130	0.060803	0.002034	0.282184	0.000023	−20.8	−18.1	1550	2337	−0.94
14	129	0.040883	0.001368	0.282257	0.000021	−18.2	−15.5	1418	2170	−0.96
15	131	0.055107	0.001723	0.282268	0.000028	−17.8	−15.1	1417	2146	−0.95
16	130	0.063219	0.002017	0.282302	0.000025	−16.6	−14.0	1380	2073	−0.94
17	128	0.047430	0.001577	0.282266	0.000024	−17.9	−15.2	1414	2152	−0.95
18	131	0.053690	0.001686	0.282222	0.000023	−19.5	−16.7	1481	2249	−0.95
07SD73 (aegirine–augite syenite)										
1	130	0.028663	0.001142	0.282223	0.000023	−19.4	−16.7	1458	2245	−0.97
2	132	0.021581	0.000876	0.282247	0.000023	−18.6	−15.8	1414	2188	−0.97
3	135	0.034900	0.001327	0.282248	0.000020	−18.5	−15.7	1430	2187	−0.96
4	134	0.030167	0.001153	0.282220	0.000025	−19.5	−16.7	1463	2249	−0.97
5	134	0.024111	0.000964	0.282200	0.000019	−20.2	−17.4	1483	2292	−0.97
6	126	0.024734	0.000991	0.282211	0.000021	−19.9	−17.2	1470	2274	−0.97
7	131	0.043310	0.001704	0.282219	0.000022	−19.6	−16.9	1486	2256	−0.95
8	132	0.016422	0.000673	0.282211	0.000020	−19.8	−17.0	1457	2268	−0.98
9	134	0.028494	0.001146	0.282176	0.000021	−21.1	−18.3	1524	2347	−0.97
10	127	0.029988	0.001197	0.282233	0.000019	−19.1	−16.4	1446	2224	−0.96
11	124	0.020849	0.000851	0.282245	0.000023	−18.6	−16.0	1416	2197	−0.97
12	131	0.029154	0.001093	0.282242	0.000020	−18.7	−16.0	1429	2201	−0.97
13	131	0.032292	0.001268	0.282214	0.000017	−19.7	−17.0	1475	2263	−0.96
14	132	0.024892	0.000994	0.282201	0.000018	−20.2	−17.4	1483	2291	−0.97
15	129	0.032764	0.001273	0.282215	0.000022	−19.7	−17.0	1474	2264	−0.96
16	128	0.040541	0.001609	0.282209	0.000020	−19.9	−17.2	1496	2279	−0.95
17	128	0.026582	0.001037	0.282207	0.000018	−20.0	−17.3	1476	2280	−0.97
18	130	0.024818	0.000993	0.282158	0.000022	−21.7	−18.9	1542	2388	−0.97
19	133	0.022457	0.000915	0.282191	0.000019	−20.5	−17.7	1493	2312	−0.97
20	127	0.030191	0.001145	0.282213	0.000020	−19.8	−17.1	1472	2268	−0.97
08LX56 (hornblende syenite)										
1	2533	0.023944	0.000786	0.281324	0.000018	−51.2	4.3	2677	2765	−0.98
2	2639	0.027672	0.000979	0.281319	0.000020	−51.4	6.1	2697	2732	−0.97
3	2430	0.016640	0.000542	0.281262	0.000019	−53.4	0.2	2744	2937	−0.98
4	2521	0.013320	0.000426	0.281272	0.000016	−53.0	2.8	2722	2847	−0.99
5	131	0.064445	0.001985	0.282263	0.000026	−18.0	−15.3	1434	2159	−0.94
6	2520	0.016155	0.000525	0.281249	0.000017	−53.9	1.8	2760	2909	−0.98
7	130	0.072900	0.002319	0.282275	0.000027	−17.6	−14.9	1430	2135	−0.93
8	130	0.146067	0.004523	0.282310	0.000029	−16.3	−13.9	1468	2067	−0.86
9	130	0.112089	0.003494	0.282219	0.000028	−19.5	−17.0	1560	2264	−0.89
10	132	0.056701	0.001829	0.282209	0.000023	−19.9	−17.2	1504	2277	−0.94
11	130	0.096215	0.003102	0.282203	0.000027	−20.1	−17.5	1567	2298	−0.91
12	2522	0.014930	0.000490	0.281276	0.000016	−52.9	2.8	2722	2846	−0.99
13	129	0.062640	0.002062	0.282232	0.000028	−19.1	−16.4	1481	2229	−0.94
14	132	0.078398	0.002339	0.282239	0.000029	−18.8	−16.2	1482	2213	−0.93
15	126	0.010928	0.000351	0.282285	0.000021	−17.2	−14.5	1342	2104	−0.99
16	130	0.156833	0.004677	0.282308	0.000027	−16.4	−13.9	1477	2071	−0.86
17	132	0.058779	0.001901	0.282289	0.000026	−17.1	−14.3	1393	2099	−0.94
18	129	0.055609	0.001839	0.282223	0.000027	−19.4	−16.7	1485	2248	−0.94
19	130	0.120804	0.003566	0.282314	0.000026	−16.2	−13.7	1422	2053	−0.89
20	129	0.047078	0.001551	0.282240	0.000030	−18.8	−16.1	1450	2210	−0.95
21	131	0.043372	0.001406	0.282252	0.000023	−18.4	−15.7	1428	2181	−0.96
22	134	0.110744	0.003386	0.282317	0.000028	−16.1	−13.5	1411	2044	−0.90
23	130	0.038936	0.001322	0.282213	0.000030	−19.8	−17.1	1479	2268	−0.96
24	129	0.066452	0.002104	0.282181	0.000027	−20.9	−18.3	1556	2343	−0.94
08LX66 (monzonite)										
1	129	0.047792	0.001423	0.282281	0.000032	−17.4	−14.7	1388	2118	−0.96
2	128	0.020901	0.000629	0.282236	0.000024	−19.0	−16.2	1420	2214	−0.98
3	128	0.047820	0.001588	0.282218	0.000023	−19.6	−16.9	1483	2260	−0.95
4	129	0.021670	0.000742	0.282236	0.000024	−19.0	−16.2	1425	2214	−0.98
5	128	0.044282	0.001504	0.282250	0.000025	−18.5	−15.8	1434	2188	−0.95
6	129	0.051434	0.001769	0.282164	0.000025	−21.5	−18.9	1567	2381	−0.95

Table 4 *(continued)*

Spot no.	Age (Ma)	$^{176}Yb/^{177}Hf$	$^{176}Lu/^{177}Hf$	$^{176}Hf/^{177}Hf$	2σ	$\varepsilon_{Hf}(0)$	$\varepsilon_{Hf}(t)$	T_{DM1} (Ma)	T_{DM2} (Ma)	$f_{Lu/Hf}$
08LX66 (monzonite)										
7	129	0.037222	0.001271	0.282276	0.000023	−17.5	−14.8	1388	2127	−0.96
8	131	0.023747	0.000790	0.282218	0.000021	−19.6	−16.8	1452	2254	−0.98
9	130	0.038280	0.001296	0.282233	0.000027	−19.0	−16.3	1449	2222	−0.96
10	131	0.023888	0.000844	0.282220	0.000027	−19.5	−16.7	1451	2250	−0.97
11	131	0.027968	0.000952	0.282211	0.000020	−19.8	−17.1	1467	2269	−0.97
12	129	0.042730	0.001463	0.282217	0.000030	−19.6	−16.9	1479	2259	−0.96
13	134	0.056361	0.001904	0.282162	0.000032	−21.6	−18.8	1575	2381	−0.94
14	131	0.028828	0.000993	0.282173	0.000025	−21.2	−18.4	1522	2355	−0.97
15	129	0.040490	0.001365	0.282241	0.000026	−18.8	−16.1	1441	2205	−0.96
16	129	0.035272	0.001228	0.282248	0.000025	−18.5	−15.8	1426	2189	−0.96
17	130	0.037657	0.001307	0.282259	0.000024	−18.1	−15.4	1414	2165	−0.96
18	131	0.030463	0.001060	0.282246	0.000031	−18.6	−15.8	1423	2193	−0.97
07SD74 (syenodiorite)										
1	133	0.021234	0.000828	0.282316	0.000018	−16.1	−13.3	1316	2033	−0.98
2	135	0.022236	0.000839	0.282283	0.000020	−17.3	−14.4	1363	2107	−0.97
3	132	0.025860	0.001004	0.282249	0.000018	−18.5	−15.7	1417	2185	−0.97
4	135	0.038995	0.001514	0.282275	0.000021	−17.6	−14.8	1399	2128	−0.95
5	132	0.041198	0.001561	0.282237	0.000021	−18.9	−16.2	1455	2215	−0.95
6	132	0.038691	0.001407	0.282257	0.000018	−18.2	−15.4	1420	2168	−0.96
8	135	0.015609	0.000621	0.282283	0.000018	−17.3	−14.4	1355	2105	−0.98
9	131	0.029946	0.001158	0.282278	0.000019	−17.5	−14.7	1382	2122	−0.97
10	130	0.031010	0.001162	0.282242	0.000018	−18.7	−16.0	1432	2202	−0.97
11	132	0.011199	0.000413	0.282256	0.000018	−18.2	−15.4	1384	2165	−0.99
12	133	0.019434	0.000719	0.282324	0.000023	−15.9	−13.0	1302	2016	−0.98
13	130	0.014409	0.000555	0.282275	0.000017	−17.6	−14.8	1364	2125	−0.98
14	129	0.024077	0.000936	0.282228	0.000022	−19.2	−16.5	1442	2232	−0.97
15	129	0.023089	0.000830	0.282286	0.000021	−17.2	−14.4	1358	2103	−0.97
16	131	0.039265	0.001351	0.282332	0.000026	−15.6	−12.8	1312	2001	−0.96
17	131	0.013311	0.000495	0.282272	0.000023	−17.7	−14.9	1367	2132	−0.99
18	141	0.076027	0.002847	0.282234	0.000029	−19.0	−16.2	1511	2222	−0.91
19	129	0.031025	0.001173	0.282277	0.000024	−17.5	−14.8	1384	2125	−0.96
20	127	0.018543	0.000693	0.282282	0.000030	−17.3	−14.6	1359	2113	−0.98

The following parameters were applied to the calculation: $(^{176}Lu/^{177}Hf)_{CHUR}=0.0332$, $(^{176}Hf/^{177}Hf)_{CHUR,0}=0.282772$, $(^{176}Lu/^{177}Hf)_{DM}=0.0384$, $(^{176}Hf/^{177}Hf)_{DM,0}=0.28325$ (Blichert-Toft and Albaréde, 1997; Griffin et al., 2000), ^{176}Lu decay constant $\lambda=1.867\times10^{-11}$ a^{-1} (Söderlund et al., 2004).

because the density would not have been sufficient. Moreover, large-scale intermediate-acid intrusions and volcanic rocks would have been produced due to direct contact between hot asthenosphere and fusible middle crust if delamination of the lower crust coupled with the lithospheric mantle had happened (Ji et al., 2008; Menzies et al., 2007). This is not observed in the Luxi Block. The Sr, Nd and Pb isotopic compositions of EM1-type rocks in the Luxi Block and Taihang Mountains are similar to each other (Figs. 5 and 6), suggesting that they share a similar mantle source. Seismic images also reveal that the mantle–crust structure of the Luxi Block is similar to the Taihang Mountains (Zhu and Zheng, 2009). Therefore, if delamination happened in Luxi Block, it must have happened in the Taihang Mountains. However, a large-scale delamination of the lower crust and lithospheric mantle in the inner NCC is highly improbable due to the refractory and buoyant properties of the cratonic mantle (Griffin et al., 1998; Menzies et al., 2007). Additionally, lithospheric delamination cannot be used to explain that the ancient refractory mantle merged with the newly accreted mantle, or the phenomena of coexistence of abundant transitional mantle, newly accreted mantle, and ancient mantle without obvious layers beneath the NCC (Zheng, 2009). The thick crust–mantle transition zone revealed by seismic images beneath the Luxi Block is also difficult to explain by delamination (Zhu and Zheng, 2009).

6.2.2. Crustal assimilation

Inherited zircons preserved in the hornblende syenite indicate that ancient crustal materials must participate in the formation of the Longbaoshan complex. The late Archean ages of the inherited zircons correspond to those of zircons from late Archean gneisses of the Luxi Block (Wang et al., 2009), further suggesting that the ancient crustal materials were derived from the basement rocks. The initial $^{87}Sr/^{86}Sr$ ratios and $\varepsilon_{Nd}(t)$ values do not increase and decrease respectively in company with increasing SiO_2 (Fig. 10a, b), implicating that assimilation of crustal materials likely occurred in the magma chamber instead of during magma ascent. More crustal materials may be involved in the aegirine–augite syenite, hornblende syenite and monzonite than in the syenodiorite and quartz syenite because of the higher initial $^{87}Sr/^{86}Sr$ ratios and lower $\varepsilon_{Nd}(t)$ values in the former group (Fig. 5). The heterogeneous lithospheric mantle, which varies from EM1- to EM2-type from northwestern to southeastern Luxi Block (Fig. 5), makes it difficult to calculate how many crustal materials were involved in the Longbaoshan complex. Given the unavailability of coexistent ultramafic rocks or peridotite enclaves to directly represent the enriched lithospheric mantle, the most primitive syenodiorite (07SD74) of the Longbaoshan complex is considered as the best candidate that reflects the isotopic characteristics of the enriched lithospheric mantle source. As a result, a simple mixing model (Langmuir et al., 1978) based on the Sr and Nd isotopes shows that the mixing of 10–35% ancient crustal materials with the enriched lithospheric mantle-derived magma can produce the observed Sr–Nd isotopic features of the aegirine–augite syenite, hornblende syenite and monzonite (Fig. 5).

6.2.3. Fractional crystallization

The very low MgO, Fe_2O_3, Cr, Co, and Ni contents (Table 2) indicate that fractional crystallization may have played an important role in the magma evolution. However, the values of δEu remain constant as SiO_2 increases (Fig. 11a) and CaO decreases (Fig. 11b), suggesting that the fractionation of plagioclase is neglectable. Separation of Ca-, Mg- and Fe-rich minerals such as hornblende and biotite may have occurred, as indicated by the negative correlation between CaO and SiO_2 (Fig. 11c), MgO and SiO_2 (Fig. 11d) and between TFe_2O_3 and SiO_2

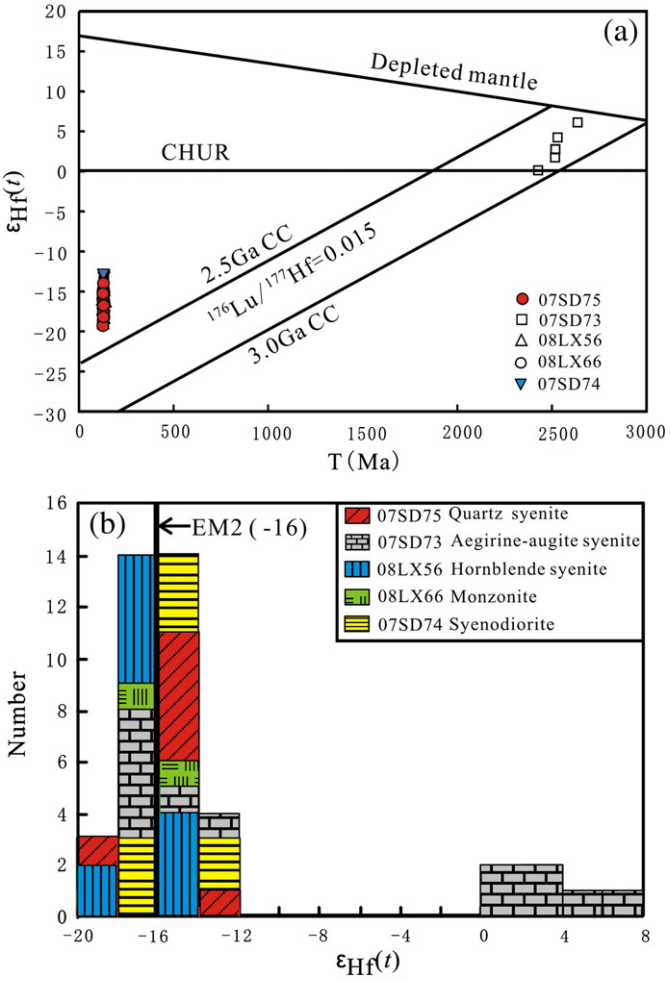

Fig. 7. Diagram of Hf isotopic evolution in zircons (a) and frequency histogram of $\varepsilon_{Hf}(t)$ for each sample analyzed (b). CHUR, chondritic uniform reservoir; CC, continental crust. Depleted mantle evolution is calculated by using $\varepsilon_{Hf}(t)=16.9$ at $t=0$ Ma and $\varepsilon_{Hf}(t)=6.4$ at $t=3.0$ Ga, the applied parameters as in Table 4. The corresponding lines of crustal extraction are calculated by using the $^{176}Lu/^{177}Hf$ ratio of 0.015 for the average continental crust (Griffin et al., 2002). Th $\varepsilon_{Hf}(t)$ value (−16) for the EM2-type lithospheric mantle beneath the Luxi Block is from Xu et al. (2007).

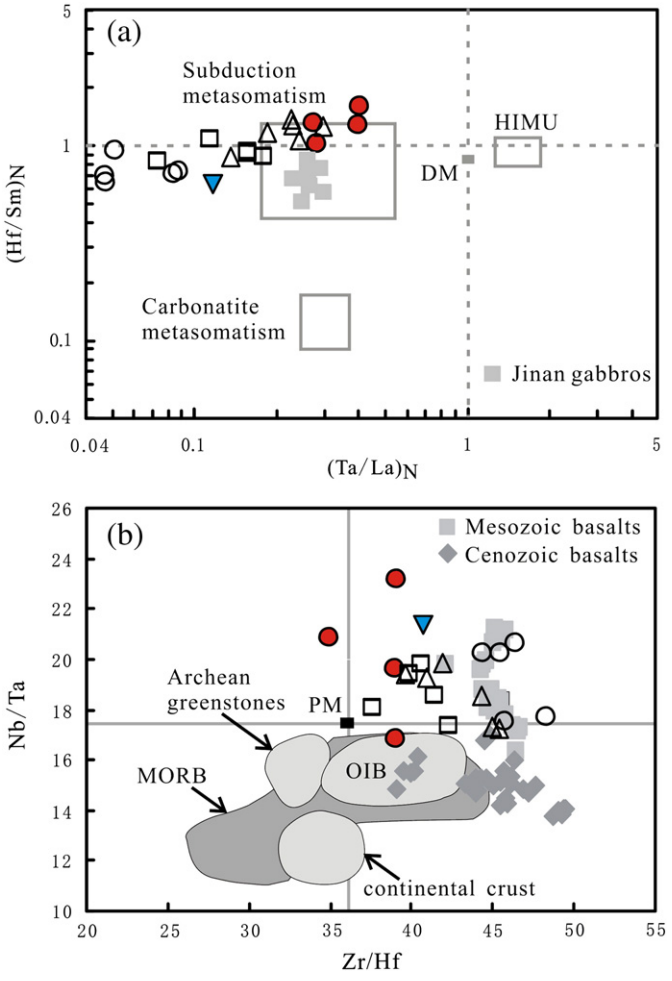

Fig. 9. (a) $(Ta/La)_N$ vs. $(Hf/Sm)_N$ diagram for the Longbaoshan complex. The trends of the subduction- and carbonatite-related metasomatism are from La Flèche et al. (1998). Jinan gabbros from the Luxi Block (Wang et al., 2006) are also shown for comparison. (b) Zr/Hf vs. Nb/Ta plot for the Longbaoshan complex. The field of PM is from Sun and McDonough (1989). Others are referred to Pfänder et al. (2007). Mesozoic and Cenozoic basalts in eastern NCC (Liu et al., 2008b) are shown for comparison. Symbols as in Fig. 3.

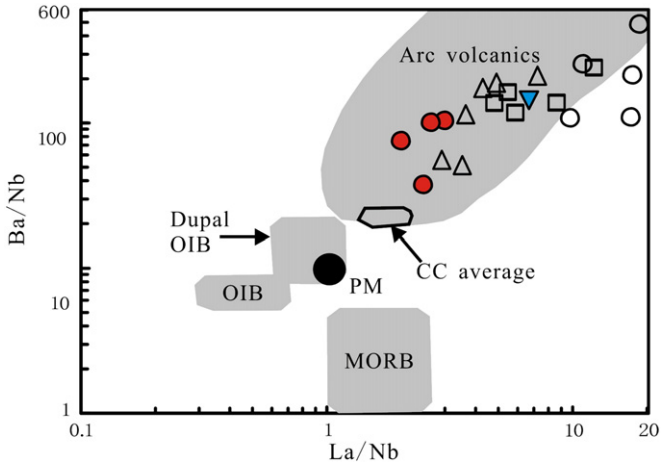

Fig. 8. Ba/Nb vs. La/Nb plot showing that the Longbaoshan complex is characterized by high Ba/Nb and La/Nb ratios, falling in the field of arc volcanics. The fields of MORB, PM, OIB, Dupal OIB, continental crust (CC) average and arc volcanics are referred to Jahn et al. (1999). Symbols as in Fig. 3.

(Fig. 11e). Fractionation of hornblende and biotite is also supported by petrographic observations in a thin section, in that there are abundant hornblende and biotite in the syenodiorite, but only rare hornblende and biotite in the quartz syenite. The sharp decrease in REE with increasing SiO_2 contents (Fig. 11f) suggests a separation of minerals with high partition coefficients of REE, such as apatite, monazite and titanite, all of which are important accessory minerals in the Longbaoshan complex. The obvious decrease of P_2O_5 with increasing SiO_2 is also consistent with removal of P-rich minerals such as apatite and monazite (Fig. 11g). The negative correlation between TiO_2 and SiO_2 (Fig. 11h) also suggests fractionation of Ti-minerals such as titanite, or ilmenite.

6.2.4. Genetic model and process

The petrogenesis of syenite is complex and many models have been proposed. Syenite petrogenesis can be generally divided into three groups based on the proposed magma source (Yang et al., 2005b and the references therein). First, syenite magmas may originate from partial melting of crustal rocks during the influx of volatiles (Azman, 2001; Martin, 2006; Miyazaki et al., 2000), or in a closed system at

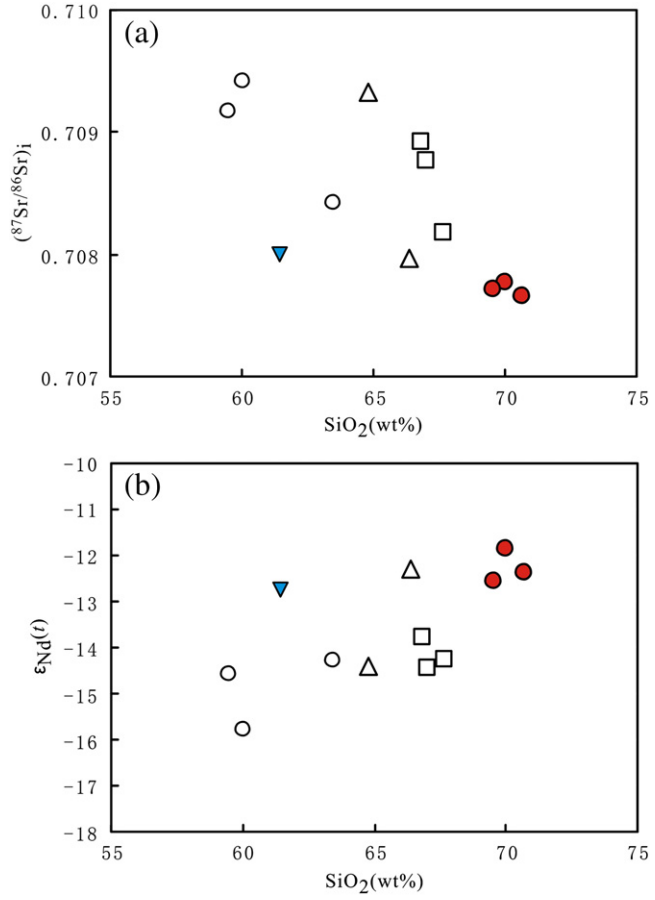

Fig. 10. Plots of initial $^{87}Sr/^{86}Sr$ ratio vs. SiO_2 (a) and $\varepsilon_{Nd}(t)$ value vs. SiO_2 (b) for the Longbaoshan alkaline complex. Symbols as in Fig. 3.

pressures typical of the base of over-thickened crust (Harris et al., 1983; Tchameni et al., 2001). Second, syenite magmas may be the products of partial melting of metasomatized/enriched mantle (Conceição and Green, 2004; Litvinovsky et al., 2002; Miyazaki et al., 2003) or differentiation of alkaline basalt magma (Brotzu et al., 2007; Macdonald and Scaillet, 2006). Third, syenites may result from magma mixing, in particular, mixing of mantle-derived silica-undersaturated alkaline mafic magmas with lower crust-derived granitic magmas (Brotzu et al., 1997; Jung et al., 2007; Zhao et al., 1995). As discussed above, the Longbaoshan complex was neither derived from crust nor purely derived from mantle. We consider that this complex originated from partial melting of the EM2-type lithospheric mantle with assimilation of ancient crustal materials. K-rich alkali magma can be produced by low-degree partial melting of a phlogopite-bearing metasomatized mantle source that was formed at the root of a subduction zone by hybridization between a slab-derived hydrous siliceous magma and the overlying mantle wedge (Wyllie and Sekine, 1982; Zhang et al., 2010). Such metasomatized mantle has a lower solidus temperature than refractory lithospheric mantle and could be preferentially melted during the initial stages of thermal perturbation during extension (Zhang et al., 2010). Partial melting of the phlogopite-bearing mantle could lead to the formation of alkaline magmatism with high K_2O and Rb abundances as observed in the Longbaoshan alkaline complex (Table 2). Ruling out the plagioclase fractionation, the Eu negative anomalies of the Longbaoshan complex (Fig. 4) may be attributed to crustal assimilation. Partial melting of the granulitic crust (Hy + Pl + Grt) would leave the residue rich in Ca-rich plagioclase and garnet and generate magma possessing a negative Eu anomaly and low HREE (Zhang et al., 2005a), which are consistent with the features of the Longbaoshan complex. Experiments have proved that Na-rich melt can be generated by 10–40% partial melting of amphibolite at pressures of ≥12 kbar (leaving a garnet granulite residue) and temperatures between 1000 and 1100 °C (Rapp and Watson, 1995). The high Na_2O contents of the Longbaoshan complex may be attributed to the assimilation of such crust-derived melt.

AFC (assimilation and crystal fractionation) (DePaolo, 1981) and MASH (melting, assimilation, storage and homogenization) (Hildreth and Moorbath, 1988) are usually proposed to describe multiple and multistage magmatic processes. In the AFC model, crustal assimilation and fractional crystallization occur synchronously during magma ascent. By contrast, crustal melting and assimilation by primary magma as well as magma storage and homogenization proceed at the base of the crust in the MASH model. From the Longbaoshan complex, the nearly identical Sr and Nd isotopic compositions between the most primitive syenodiorite and felsic quartz syenite suggest that fractional crystallization instead of crustal contamination dominated during magma ascent. The higher initial $^{87}Sr/^{86}Sr$ ratios and lower $\varepsilon_{Nd}(t)$ values but lower SiO_2 contents of the aegirine–augite syenite, hornblende syenite and monzonite also oppose to crustal contamination occurring during magma ascent. Therefore, we consider that crustal assimilation in the Longbaoshan complex is different from the AFC process, but similar to the MASH process. That is to say, enriched lithospheric mantle-derived alkaline magma was unevenly contaminated by crust-derived melt in the magma chamber, producing the somewhat inhomogeneous parental magma of the Longbaoshan complex.

Based on the above discussion, a scenario for the origin of the Longbaoshan complex can be described as follows: before 130 Ma, the lithospheric mantle was modified by the subducted Yangtze continental crust and transformed into EM2-type counterpart in the southeastern Luxi Block. At ~130 Ma, partial melting of the EM2-type lithospheric mantle produced K-rich alkaline magma, which was characterized by LREE and LILE's enrichment and HFSE's depletion. This magma underplated the ancient crust of the Luxi Block and assimilated the crust-derived melt through MASH process, forming the Longbaoshan parental magma, which was emplaced at a shallow crustal level after fractionation of hornblende, biotite, apatite/monazite and titanite.

6.3. Geodynamic significance

Extensional tectonics, driving development of northwestward downfaulted basins and radial or concentric ring faults, progressed in the Luxi Block during the early Cretaceous. Intrusions within the research area were mainly controlled by extensional tectonics. Subduction of the Yangtze continental crust, which collided with the NCC during the Triassic, could not have been the driving force behind development of this tectonic environment because of the large difference in time, but may have played an important role in modifying the lithospheric mantle beneath the southeastern NCC (Zhang et al., 2005a, 2005b). Development of this extensional regime was coeval with the Mesozoic tectonic inversion in the eastern NCC, indicating that extensional tectonics in the Luxi Block was also controlled by the local tectonic regime in the eastern NCC. The tectonic regime in the eastern NCC sharply transformed from compressional to extensional from 150–100 Ma (peak of 120 Ma, Zhai et al., 2004a, 2004b). This inversion may be the delayed result of collision or subduction between NCC and surrounding geological terranes (Xu et al., 2009; Zhai et al., 2004b), such as the Triassic collision between the NCC and the Yangtze Craton, the mid to late Jurassic collision of the Siberia Craton with the combined NCC and Mongolian continents (Meng, 2003), and the early Cretaceous subduction of Paleo-Pacific slab underneath the eastern Asian continent. However, subduction of the Paleo-Pacific slab may have played a critical role in this process (Sun et al., 2007; Xu et al., 2009). Back-arc extension and sinistral slip movement of the Tan-Lu fault induced by

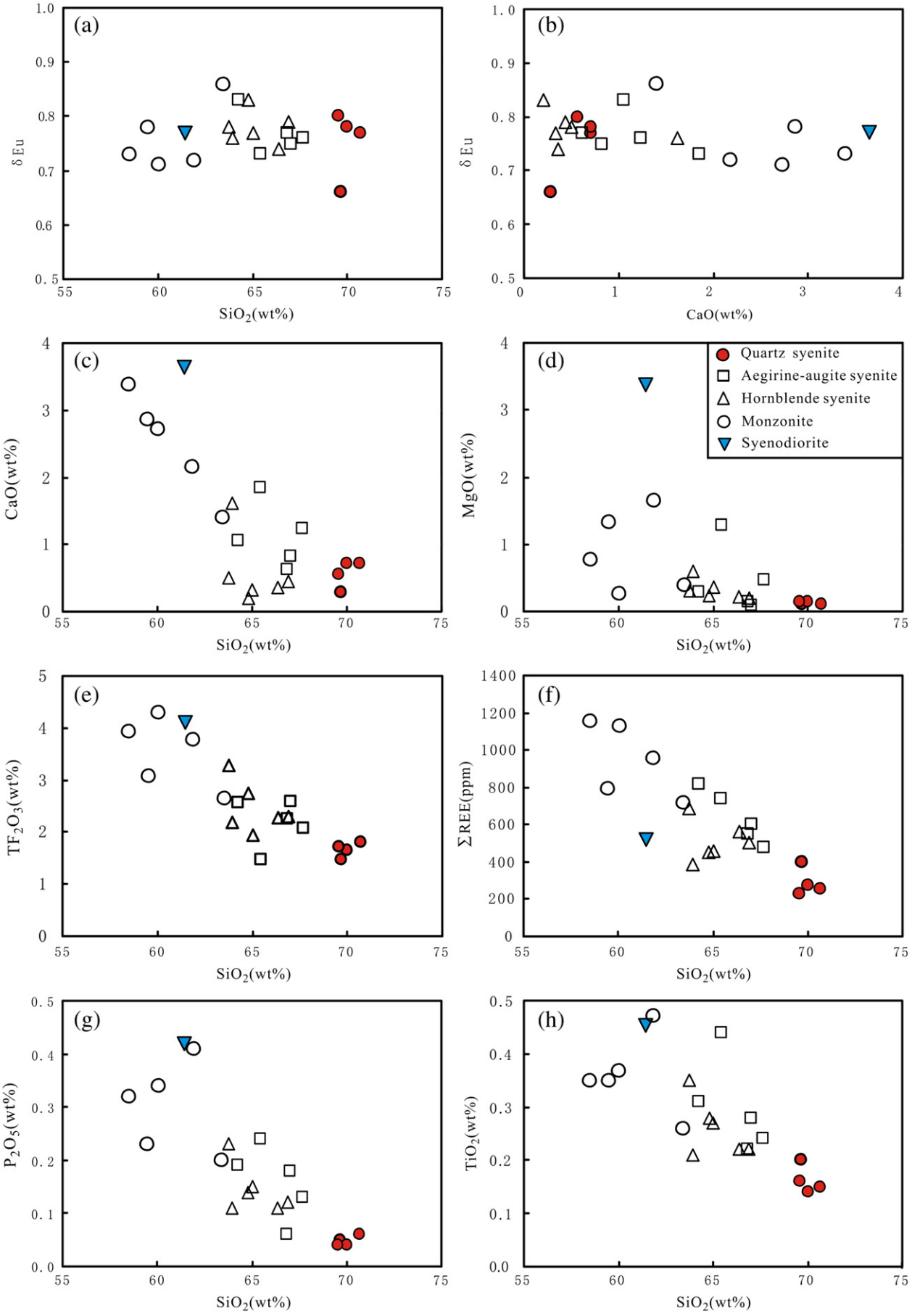
(a)
δ Eu
SiO2(wt%)
(b)
δ Eu
CaO(wt%)
(c)
CaO(wt%)
SiO2(wt%)
(d)
MgO(wt%)
SiO2(wt%)
Quartz syenite
Aegirine-augite syenite
Hornblende syenite
Monzonite
Syenodiorite
(e)
TF2O3(wt%)
SiO2(wt%)
(f)
ΣREE(ppm)
SiO2(wt%)
(g)
P2O5(wt%)
SiO2(wt%)
(h)
TiO2(wt%)
SiO2(wt%)

the Paleo-Pacific subduction in the early Cretaceous caused intense extension of lithospheric mantle and upwelling of the asthenosphere (Chen et al., 2005; Sun et al., 2007; Zhang et al., 2003, 2005b; Zheng, 2009), resulting in development of extensional tectonics and magmatic activities at shallow crustal levels.

6.4. Implications for destruction of the NCC

During the formation of the Longbaoshan complex, two stages of crust–mantle interaction can be identified. Firstly, the lithospheric mantle was metasomatized by the melts/fluids derived from the subducted Yangtze crust and then transformed into an EM2 counterpart; secondly, magma derived from the EM2 source underplated the lower crust and assimilated the crust-derived materials. Experimental results have shown that silica-saturated melt derived from eclogite will react with mantle peridotite to form pyroxenite or garnet pyroxenite (Kogiso and Hirschmann, 2001; Kogiso et al., 2003; Rapp et al., 1999; Sobolev et al., 2007; Yaxley, 2000). Melting temperatures of pyroxenite and garnet pyroxenite are lower than those of mantle peridotite. As a result, formation of pyroxenite and garnet pyroxenite will induce mantle melting (Gao et al., 2009). Thus, the first stage crust–mantle interaction greatly changed the compositions of the lithospheric mantle, and destroyed its stability, making it easy to melt. The second stage crust–mantle interaction was also widely observed in the Mesozoic magmatic rocks in the NCC. AFC, MASH and magma mixing are the potential processes for the crustal assimilation. Magmatic underplating may have played an important role in these processes. The thick crust–mantle transition zone and fuzzy mantle–crust boundary revealed by seismic images of the Luxi Block (Zhu and Zheng, 2009) indicate that magmatic underplating did occur. Researches on lower crust granulite xenoliths and garnet pyroxenite xenoliths from the Hannuoba Cenozoic basalts in the central NCC suggest that intense magmatic underplating occurred during 140–120 Ma and that the Archean lower crust was probably replaced by the Mesozoic lower crust (Fan et al., 2005; Zhai et al., 2007).

According to the above discussion, we propose that multiple crust–mantle interaction is the essential mechanism for the destruction of the NCC. The first intensive crust–mantle interaction was invoked by crust subduction and was responsible for the lithospheric mantle destruction, the second major crust–mantle interaction was induced by mantle-derived magma underplating and was responsible for the crust destruction/activation. Occurrence of the Longbaoshan complex indicates both of the above crust–mantle interaction operated in the Luxi Block. However, from northwest to southeast, the lithospheric mantle beneath the Luxi Block changed from EM1-type to EM2-type, suggesting that crustal modification on lithospheric mantle became stronger in the southeastern Luxi Block, which may be attributed to the deep-rooted Tan-Lu fault and the closer distance to the suture between the NCC and the YC.

7. Conclusions

1. The Longbaoshan complex was emplaced in the early Cretaceous (129.4–131.7 Ma), and contains inherited zircons with ages from 2.51 to 2.64 Ga.
2. The Longbaoshan complex originated from partial melting of the EM2-type lithospheric mantle with assimilation of ancient crustal materials. The enriched mantle source was produced by modification of the melts/fluids derived from the subducting Yangtze crust. MASH process was the most possible way for the crustal assimilation.
3. The Longbaoshan complex developed in an extensional setting that resulted from subduction of the Paleo-Pacific slab and upwelling of the asthenosphere.
4. Based on this study, we propose that multiple crust–mantle interaction is the essential mechanism for the destruction of the NCC. The lithospheric mantle destruction was invoked by crust subduction and the crustal activation was induced by mantle-derived magma underplating.

Acknowledgements

This paper was significantly improved by comments of Haibo Zou, Teal Riley as well as by editorial comments and helpful suggestions of Andrew Kerr. We are grateful to Chao-Feng Li and Xiang-hui Li for helping analyze Sr, Nd and Pb isotopes, and Zhao-Chu Hu for helping with zircon LA–ICP-MS dating. We are also thankful to Stephanie E. Mills for her very careful English editorial work for the early version. This study was financially supported by the Natural Science Foundation of China (40625010 and 40702016) and the Crisis Mines Continued Resources Exploration Project of China Geological Survey (20089930).

References

Azman, A.G., 2001. Petrology and geochemistry of granite and syenite from Perhentian Island, Peninsular Malaysia. Geosciences Journal 5, 123–137.
Barry, T.L., Kent, R.W., 1998. Cenozoic magmatism in Mongolia and the origin of central and east Asian basalts. In: Flower, M.F.J., Chung, S.L., Lo, C.H., Lee, T.Y. (Eds.), Mantle Dynamics and Plate Interactions in East Asia. Geodynamics Series. American Geophysical Union, pp. 347–364.
Barth, M.G., McDonough, W.F., Rudnick, R.L., 2000. Tracking the budget of Nb and Ta in the continental crust. Chemical Geology 165, 197–213.
Blichert-Toft, J., Albaréde, F., 1997. The Lu–Hf isotope geochemistry of chondrites and the evolution of the mantle–crust system. Earth and Planetary Science Letters 148, 243–258.
Bonin, B., Azzouni-Sekkal, A., Bussy, F., Ferrag, S., 1998. Alkali–calcic and alkaline post-orogenic (PO) granite magmatism: petrologic constraints and geodynamic settings. Lithos 45, 45–70.
Bromiley, G.D., Reffern, S.A.T., 2008. The role of TiO_2 phases during melting of subduction-modified crust: implications for deep mantle melting. Earth and Planetary Science Letters 267, 301–308.
Brotzu, P., Gomes, C.B., Melluso, L., Morbidelli, L., Morra, V., Ruberti, E., 1997. Petrogenesis of coexisting SiO_2-undersaturated to SiO_2-oversaturated felsic igneous rocks: the alkaline complex of Itatiaia, southeastern Brazil. Lithos 40, 133–156.
Brotzu, P., Melluso, L., Bennio, L., Gomes, C.B., Lustrino, M., Morbidelli, L., Morra, V., Ruberti, E., Tassinari, C., D'Antonio, M., 2007. Petrogenesis of the Early Cenozoic potassic alkaline complex of Morro de São João, southeastern Brazil. Journal of South American Earth Sciences 24, 93–115.
Chen, B., Zhai, M.G., 2003. Geochemistry of late Mesozoic lamprophyre dykes from the Taihang Mountains, north China and implications for the sub-continental lithospheric mantle. Geological Magazine 140, 87–93.
Chen, L.H., Zhou, X.H., 2004. Ultramafic xenoliths in Mesozoic diorite in west Shandong Province. Science in China (Series D) 47, 489–499.
Chen, B., Jahn, B.M., Zhai, M.G., 2003. Sr–Nd isotopic characteristics of the Mesozoic magmatism in the Taihang–Yanshan orogen, north China craton and implications for Archean lithosphere thinning. Journal of the Geological Society of London 160, 963–970.
Chen, B., Jahn, B.M., Arakawa, Y., Zhai, M.G., 2004. Petrogenesis of the Mesozoic intrusive complexes from the southern Taihang orogen, North China Craton: elemental and Sr–Nd–Pb isotopic constraints. Contributions to Mineralogy and Petrology 148, 489–501.
Chen, B., Tian, W., Zhai, M.G., Arakawa, Y., 2005. Zircon U–Pb geochronology and geochemistry of the Mesozoic magmatism in the Taihang Mountains and other places of the North China Craton, with implications for petrogenesis and geodynamic setting. Acta Petrologica Sinica 21, 13–24 (in Chinese with English abstract).
Chen, B., Tian, W., Jahn, B.M., Chen, Z.C., 2008a. Zircon SHRIMP U–Pb ages and in-situ Hf isotopic analysis for the Mesozoic intrusions in South Taihang, North China Craton: evidence for hybridization between mantle-derived magmas and crustal components. Lithos 102, 118–137.
Chen, L., Tao, W., Zhao, L., Zhen, T.Y., 2008b. Distinct lateral variation of lithospheric thickness in the Northeastern North China Craton. Earth and Planetary Science Letters 267, 56–68.

Fig. 11. Plots of δEu vs. SiO_2 (a) and δEu vs. CaO (b) indicate that plagioclase fractionation was insignificant. Plots of CaO vs. SiO_2 (c), MgO vs. SiO_2 (d) and TFe_2O_3 vs. SiO_2 (e) suggest that amphibole and biotite may fractionate from the magma. Plots of $\sum$ REE vs. SiO_2 (f) and P_2O_5 vs. SiO_2 (g) imply that fractionation of apatite and/or monazite may have occurred. Plot of TiO_2 vs. SiO_2 (h) indicates that Ti-rich minerals such as titanite may have fractionated from the magma.

Chu, Z.Y., Wu, F.Y., Walker, R.J., Rudnick, R.L., Pitcher, L., Puchtel, I.S., Yang, Y.H., Wilde, S.A., 2009. Temporal evolution of the lithospheric mantle beneath the eastern North China Craton. Journal of Petrology 50, 1857–1898.

Conceição, R.V., Green, D.H., 2004. Derivation of potassic (shoshonitic) magmas by decompression melting of phlogopite + pargasite lherzolite. Lithos 72, 209–229.

De la Roche, H., Leterrier, J., Granclaude, P., Marchal, M., 1980. A classification of volcanic and plutonic rocks using R1–R2 diagram and major-element analyses—its relationships with current nomenclature. Chemical Geology 29, 183–210.

Deng, J.F., Su, S.G., Niu, Y.L., Liu, C., Zhao, G.C., Zhao, X.G., Zhou, S., Wu, Z.X., 2007. A possible model for the lithospheric thinning of North China Craton: evidence from the Yanshanian (Jura-Cretaceous) magmatism and tectonism. Lithos 96, 22–35.

DePaolo, D.J., 1981. Trace element and isotopic effects of combined wallrock assimilation and fractional crystallization. Earth and Planetary Science Letters 53, 189–202.

Fan, W.M., Zhang, H.F., Baker, J., Jarvis, K.E., Mason, P.R.D., Menzies, M.A., 2000. On and off the North China Craton: where is the Archaean keel? Journal of Petrology 41, 933–950.

Fan, Q.C., Zhang, H.F., Sui, J.L., Zhai, M.G., Sun, Q., Li, N., 2005. Magma underplating and Hannuoba present crust–mantle transitional zone composition: xenolith petrological and geochemical evidence. Science in China (Series D) 48 (8), 1089–1105.

Foley, S.F., Barth, M.G., Jenner, G.A., 2000. Rutile/melt partition coefficients for trace elements and an assessment of the influence of rutile on the trace element characteristics of subduction zone magmas. Geochimica et Cosmochimica Acta 64, 933–938.

Furukawa, Y., Tatsumi, Y., 1999. Melting of a subducting slab and production of high-Mg andesite magmas: unusual magmatism in SW Japan. Geophysical Research Letters 26, 2271–2274.

Galer, S.J.G., Abouchami, W., 1998. Practical application of lead triple spiking for correction of instrumental mass discrimination. Mineralogical Magazine 62A, 491–492.

Gao, S., Rudnick, R.L., Yuan, H.L., Liu, X.M., Liu, Y.S., Xu, W.L., Ling, W.L., Ayers, J., Wang, X.C., Wang, Q.H., 2004. Recycling lower continental crust in the North China Craton. Nature 432, 892–897.

Gao, S., Rudnick, R.L., Xu, W.L., Yuan, H.L., Liu, Y.S., Walker, R.J., Puchtel, I., Liu, X.M., Huang, H., Wang, X.R., Yang, J., 2008. Recycling deep cratonic lithosphere and generation of intraplate magmatism in the North China Craton. Earth and Planetary Science Letters 270, 41–53.

Gao, S., Zhang, J.F., Xu, W.L., Liu, Y.S., 2009. Delamination and destruction of the North China Craton. Chinese Science Bulletin 54, 3367–3378.

Goolaerts, A., Mattielli, N., Jong, J.D., Weis, D., Scoatea, J.S., 2004. Hf and Lu isotopic reference values for the zircon standard 91500 by MC–ICP-MS. Chemical Geology 206, 1–9.

Green, T.H., 1995. Significance of Nb/Ta as an indicator of geochemical processes in the crust–mantle system. Chemical Geology 120, 347–359.

Green, T.H., Pearson, N.J., 1987. An experimental study of Nb and Ta partitioning between Ti-rich minerals and silicate liquids at high pressure and temperature. Geochimica et Cosmochimica Acta 51, 55–62.

Griffin, W.L., Zhang, A.D., O'Reilly, S.Y., Ryan, C.G., 1998. Phanerozoic evolution of the lithosphere beneath the Sino-Korean Craton. In: Flower, M.F.J., Chung, S.L., Lo, C.H., Lee, T.Y. (Eds.), Mantle Dynamics and Plate Interactions in East Asia. Geodynamic Series. American Geophysical Union, Washington, D.C., pp. 107–126.

Griffin, W.L., Pearson, N.J., Belousova, E., Jackson, S.E., Achterbergh, E.V., O'Reilly, S.Y., Shee, S.R., 2000. The Hf isotope composition of cratonic mantle: LAM–MC–ICPMS analysis of zircon megacrysts in kimberlites. Geochimica et Cosmochimica Acta 64, 133–147.

Griffin, W.L., Wang, X., Jackson, S.E., Pearson, N.J., O'Reilly, S.Y., Xu, X.S., Zhou, X.M., 2002. Zircon chemistry and magma mixing, SE China: in-situ analysis of Hf isotopes, Tonglu and Pingtan igneous complexes. Lithos 61, 237–269.

Guo, F., Fan, W.M., Wang, Y.J., 2001. Late Mesozoic mafic intrusive complexes in North China Block: constraints on the nature of subcontinental lithospheric mantle. Physics and Chemistry of the Earth (Part A: Solid Earth and Geodesy) 26, 759–771.

Harris, N.B.W., Duyverman, H.J., Almond, D.C., 1983. The trace element and isotope geochemistry of the Sabaloka igneous complex, Sudan. Journal of the Geological Society of London 140, 245–256.

Hart, S.R., 1984. A large-scale isotope anomaly in the southern hemisphere mantle. Nature 309, 753–757.

Hildreth, W., Moorbath, S., 1988. Crustal contributions to arc magmatism in the Andes of central Chile. Contributions to Mineralogy and Petrology 98, 455–489.

Jacob, D.E., 2004. Nature and origin of eclogite xenoliths from kimberlites. Lithos 77, 295–316.

Jahn, B.M., Auvray, B., Shen, Q.H., Liu, D.Y., Zhang, Z.Q., Dong, Y.J., Ye, X.J., Zhang, Q.Z., Cornichet, J., Mace, J., 1988. Archean crustal evolution in China: the Taishan complex, and evidence for juvenile crustal addition from long-term depleted mantle. Precambrian Research 38, 381–403.

Jahn, B.M., Wu, F.Y., Lo, C.H., Tsai, C.H., 1999. Crust–mantle interaction induced by deep subduction of the continental crust: geochemical and Sr–Nd isotopic evidence from post-collisional mafic–ultramafic intrusions of the northern Dabie complex, central China. Chemical Geology 157, 119–146.

Ji, S.Z., Wang, Q., Xu, Z.Q., 2008. Break-up of the North China Craton through lithospheric thinning. Acta Geologica Sinica 82, 174–193 (in Chinese with English abstract).

Jung, S., Hoffer, E., Hoernes, S., 2007. Neo-Proterozoic rift-related syenites (Northern Damara Belt, Namibia): geochemical and Nd–Sr–Pb–O isotope constraints for mantle sources and petrogenesis. Lithos 96, 415–435.

Kamber, B.S., Collerson, K.D., 2000. Role of 'hidden' deeply subducted slabs in mantle depletion. Chemical Geology 166, 241–254.

Kamei, A., Owada, M., Nagao, T., Shiraki, K., 2004. High-Mg diorites derived from sanukitic HMA magmas, Kyushu Island, southwest Japan arc: evidence from clinopyroxene and whole rock compositions. Lithos 75, 359–371.

Klemme, S., Prowatke, S., Hametner, K., Gunther, D., 2005. Partitioning of trace elements between rutile and silicate melts: implications for subduction zones. Geochimica et Cosmochimica Acta 69, 2361–2371.

Kogiso, T., Hirschmann, M.M., 2001. Experimental study of clinopyroxenite partial melting and the origin of ultra-calcic melt inclusions. Contributions to Mineralogy and Petrology 142, 347–360.

Kogiso, T., Hirschmann, M.M., Frost, D.J., 2003. High-pressure partial melting of garnet pyroxenite: possible mafic lithologies in the source of ocean island basalts. Earth and Planetary Science Letters 216, 603–617.

La Flèche, M.R., Camire, G., Jenner, G.A., 1998. Geochemistry of post-Acadian, Carboniferous continental intraplate basalts from the Maritimes Basin, Magdalen Islands, Quebec, Canada. Chemical Geology 148, 115–136.

Langmuir, C.H., Vocke, R.D., Hanson, G.N., 1978. A general mixing equation with applications to Icelandic basalts. Earth and Planetary Science Letters 37, 380–392.

Li, S.G., Xiao, Y.L., Liou, D.L., Chen, Y.Z., Ge, N.J., Zhang, Z.Q., Sun, S.S., Cong, B.L., Zhang, R.Y., Hart, S.R., Wang, S.S., 1993. Collision of the North China and Yangtze blocks and formation of coesite-bearing eclogites: timing and process. Chemical Geology 109, 89–111.

Li, S.G., Nie, Y.H., Hart, S.R., Zhang, Z.Q., 1998. Interaction between subducted continental crust and the mantle-II. Sr and Nd isotopic geochemistry of the syncollisional mafic–ultramafic intrusions in Dabie Mountains. Science in China (Series D) 41, 632–638.

Li, Q.Z., Xie, Z., Chen, J.F., Gao, T.S., Yu, G., Qian, H., 2007. Pb–Sr–Nd isotopic characteristics of the gabbros from Jinan and Zouping and the contribution of the lower crust to the magma source. Geological Journal of China Universities 13, 297–310 (in Chinese with English abstract).

Liang, J.L., Ding, X., Sun, X.M., Zhang, Z.M., Zhang, H., Sun, W.D., 2009. Nb/Ta fractionation observed in eclogites from the Chinese Continental Scientific Drilling Project. Chemical Geology 268, 27–40.

Liégeois, J.P., Navez, J., Hertogen, J., Black, R., 1998. Contrasting origin of post-collisional high-K calc-alkaline and shoshonitic versus alkaline and peralkaline granitoids. The use of sliding normalization. Lithos 45, 1–28.

Litvinovsky, B.A., Jahn, B.M., Zanvilevich, A.N., Shadaev, M.G., 2002. Crystal fractionation in the petrogenesis of an alkali monzodiorite–syenite series: the Oshurkovo plutonic sheeted complex, Transbaikalia, Russia. Lithos 64, 97–130.

Liu, Y.S., Gao, S., 2007. High Nb/Ta ratios of the Mesozoic basalts from North China: records of continental crust recycling. Bulletin of Mineralogy, Petrology and Geochemistry 26, 19–28 (in Chinese with English abstract).

Liu, S., Hu, R.Z., Gao, S., Feng, C.X., Qi, L., Zhong, H., Xiao, T.F., Qi, Y.Q., Wang, T., Coulson, L.M., 2008a. Zircon U–Pb geochronology and major, trace elemental and Sr–Nd–Pb isotopic geochemistry of mafic dykes in western Shandong Province, East China: constrains on their petrogenesis and geodynamic significance. Chemical Geology 255, 329–345.

Liu, Y.S., Gao, S., Kelemen, P.B., Xu, W.L., 2008b. Recycled lower continental crust controls contrasting source compositions of Mesozoic and Cenozoic basalts in Eastern China. Geochimica et Cosmochimica Acta 72, 2349–2376.

Liu, Y.S., Hu, Z.C., Gao, S., Günther, D., Xu, J., Gao, C.G., Chen, H.H., 2008c. In situ analysis of major and trace elements of anhydrous minerals by LA–ICP-MS without applying an internal standard. Chemical Geology 257, 34–43.

Liu, Y.S., Gao, S., Hu, Z.C., Gao, C.G., Zong, K., Wang, D., 2010. Continental and oceanic crust recycling-induced melt–peridotite interactions in the Trans-North China Orogen: U–Pb dating, Hf isotopes and trace elements in zircons of mantle xenoliths. Journal of Petrology 51, 537–571.

Ludwig, K.R., 2003. User's Manual for Isoplot 3.00, a Geochronolgical Toolkit for Microsoft Excel. Berkeley Geochronological Center Special Publication No. 4, pp. 25–32.

Lugmair, G.W., Harti, K., 1978. Lunar initial $^{143}Nd/^{144}Nd$: differential evolution of the lunar crust and mantle. Earth and Planetary Science Letters 39, 349–357.

Macdonald, R., Scaillet, B., 2006. The central Kenya peralkaline province: insights into the evolution of peralkaline salic magmas. Lithos 91, 59–73.

Martin, R.F., 2006. A-type granites of crustal origin ultimately result from open-system fenitization-type reactions in an extensional environment. Lithos 91, 125–136.

Meng, Q.R., 2003. What drove late Mesozoic extension of the northern China–Mongolia tract? Tectonophysics 369, 155–174.

Menzies, M.A., Fan, W.M., Zhang, M., 1993. Palaeozoic and Cenozoic lithoprobes and the loss of >120 km of Archaean lithosphere, Sino-Korean craton, China. In: Prichard, H.M., Alabaster, T., Harris, N.B.W., Neary, C.R. (Eds.), Magmatic Processes and Plate Tectonics. Geological Society Special Publication, pp. 71–78.

Menzies, M., Xu, Y.G., Zhang, H.F., Fan, W.M., 2007. Integration of geology, geophysics and geochemistry: a key to understanding the North China Craton. Lithos 96, 1–21.

Miyazaki, T., Kagami, H., Shuto, K., Mohan, V.R., Rajasekaran, K.C., 2000. Rb–Sr geochronology, Nd–Sr isotopes and whole rock geochemistry of Yelagiri and Sevattur syenites, Tamil Nadu, South India. Gondwana Research 3, 39–53.

Miyazaki, T., Kagami, H., Mohan, V.R., Shuto, K., Morikiyo, T., 2003. Enriched subcontinental lithospheric mantle in the northern part of the South Indian Granulite Terrain: evidence from Yelagiri and Sevattur Syenite Plutons, Tamil Nadu, South India. Gondwana Research 6, 585–594.

Pfänder, J.A., Münker, C., Stracke, A., Mezger, K., 2007. Nb/Ta and Zr/Hf in ocean island basalts—implications for crust–mantle differentiation and the fate of Niobium. Earth and Planetary Science Letters 254, 158–172.

Qiu, J.S., Hu, J., Jiang, S.Y., Wang, R.C., Xu, X.S., 2005. Mesozoic–Cenozoic mafic magmatism in western Shandong Province and its implication for the chemical evolution of the mantle. Earth Science-Journal of China University of Geosciences 30, 646–658 (in Chinese with English abstract).

Rapp, R.P., Watson, E.B., 1995. Dehydration melting of metabasalt at 8–32 kbar: implications for continental growth and crust–mantle recycling. Journal of Petrology 36, 891–931.

Rapp, R.P., Shimizu, N., Norman, M.D., Applegate, G.S., 1999. Reaction between slab-derived melts and peridotite in the mantle wedge: experimental constraints at 3.8 GPa. Chemical Geology 160, 335–356.

Rudnick, R.L., Barth, M., Horn, I., McDonough, W.F., 2000. Rutile-bearing refractory eclogites: missing link between continents and depleted mantle. Science 287, 278–281.

Schmidt, M.W., Dardon, A., Chazot, G., Vannucci, R., 2004. The dependence of Nb and Ta rutile–melt partitioning on melt composition and Nb/Ta fractionation during subduction processes. Earth and Planetary Science Letters 226, 415–432.

Shellnutt, J.G., Zhou, M.F., 2008. Permian, rifting related fayalite syenite in the Panxi region, SW China. Lithos 101, 54–73.

Sobolev, A.V., Hofmann, A.W., Kuzmin, D.V., et al., 2007. The amount of recycled crust in sources of mantle-derived melts. Science 316, 412–417.

Söderlund, U., Patchett, P.J., Vervoort, J.D., Isachsen, C.E., 2004. The ^{176}Lu decay constant determined by Lu–Hf and U–Pb isotope systematics of Precambrian mafic intrusions. Earth and Planetary Science Letters 219, 311–324.

Steiger, R.H., Jäger, E., 1977. Subcommission on geochronology: convention on the use of decay constants in geo- and cosmochronology. Earth and Planetary Science Letters 36, 359–362.

Sun, S.S., McDonough, W.F., 1989. Chemical and isotopic systematics of oceanic basalts: implications for mantle composition and processes. In: Saunders, A.D., Norry, M.J. (Eds.), Magmatism in the Oceanic Basalts. Geological Society Special Publication, pp. 313–345.

Sun, W.D., Ding, X., Hu, Y.H., Li, X.H., 2007. The golden transformation of the Cretaceous plate subduction in the west Pacific. Earth and Planetary Science Letters 262, 533–542.

Taylor, S.R., McLennan, S.M., 1985. The Continental Crust: its Composition and Evolution. Blackwell, Oxford, pp. 1–312.

Tchameni, R., Mezger, K., Nsifa, N.E., Pouclet, A., 2001. Crustal origin of early Proterozoic syenites in the Congo Craton (Ntem Complex), South Cameroon. Lithos 57, 3–42.

Upadhyay, D., Raith, M.M., Mezger, K., Hammerschmidt, K., 2006. Mesoproterozoic rift-related alkaline magmatism at Elchuru, Prakasam Alkaline Province, SE India. Lithos 89, 447–477.

Wang, Y.J., Fan, W.M., Zhang, H.F., Peng, T.P., 2006. Early Cretaceous gabbroic rocks from the Taihang Mountains: implications for a paleosubduction-related lithospheric mantle beneath the central North China Craton. Lithos 86, 281–302.

Wang, S.J., Wan, Y.S., Zhang, C.J., Yang, E.X., Song, Z.Y., Wang, L.F., Wang, J.G., 2009. Forming ages of early Precambrian metamorphic strata in Shandong Province—proofs of zircon SHRIMP U–Pb dating. Shandong Land and Resources 25 (10), 18–24 (in Chinese with English abstract).

Wiedenbeck, M., Alle, P., Corfu, F., Griffin, W.L., Meier, M., Oberli, F., Quadt, A.V., Roddick, J.C., Spiegel, W., 1995. Three natural zircon standards for U–Th–Pb, Lu–Hf, trace element and REE analyses. Geostandards and Geoanalytical Research 19, 1–23.

Wilde, S.A., Zhou, X.H., Nemchin, A.A., Sun, M., 2003. Mesozoic crust–mantle interaction beneath the North China Craton: a consequence of the dispersal of Gondwanaland and accretion of Asia. Geology 31, 817–820.

Wu, X.Y., Xu, Y.G., Ma, J.L., Xu, J.F., Wang, Q., 2003. Geochemistry and petrogenesis of the Mesozoic high-Mg diorites from western Shandong. Geotectonica et Metallogenia 27, 228–236 (in Chinese with English abstract).

Wu, F.Y., Lin, J.Q., Wilde, S.A., Zhang, X.O., Yang, J.H., 2005. Nature and significance of the Early Cretaceous giant igneous event in eastern China. Earth and Planetary Science Letters 233, 103–119.

Wyllie, P.J., Sekine, T., 1982. The formation of mantle phlogopite in subduction zone hybridization. Contributions to Mineralogy and Petrology 79, 375–380.

Xie, L.W., Zhang, Y.B., Sun, J.F., Wu, F.Y., 2008. In situ simultaneous determination of trace elements, U–Pb and Lu–Hf isotopes in zircon and baddeleyite. Chinese Science Bulletin 53, 1565–1573.

Xiong, X.L., Adam, J., Green, T.H., 2005. Rutile stability and rutile/melt HFSE partitioning during partial melting of hydrous basalt: implications for TTG genesis. Chemical Geology 218, 339–359.

Xu, Y.G., 2001. Thermo-tectonic destruction of the Archean lithospheric keel beneath the Sino-Korean Craton: evidence, timing and mechanism. Physics and Chemistry of the Earth (Part A: Solid Earth and Geodesy) 26, 747–757.

Xu, Y.G., Huang, X.L., Ma, J.L., Wang, Y.B., Iizuka, Y., Xu, J.F., Wang, Q., Wu, X.Y., 2004a. Crust–mantle interaction during the tectono–thermal reactivation of the North China Craton: constraints from SHRIMP zircon U–Pb chronology and geochemistry of Mesozoic plutons from western Shandong. Contributions to Mineralogy and Petrology 147, 750–767.

Xu, Y.G., Ma, J.L., Huang, X.L., Iizuka, Y., Chung, S.L., Wang, Y.B., Wu, X.Y., 2004b. Early Cretaceous gabbroic complex from Yinan, Shandong Province: petrogenesis and mantle domains beneath the North China Craton. International Journal of Earth Sciences 93, 1025–1041.

Xu, W.L., Gao, S., Wang, Q.H., Wang, D.Y., Liu, Y.S., 2006. Mesozoic crustal thickening of the eastern North China Craton: evidence from eclogite xenoliths and petrologic implications. Geology 34, 721–724.

Xu, Y.G., Wu, X.Y., Luo, Z.Y., Ma, J.L., Huang, X.L., Xie, L.W., 2007. Zircon Hf isotope compositions of Middle Jurassic–Early Cretaceous intrusions in Shandong Province and its implications. Acta Petrologica Sinica 23 (2), 307–316 (in Chinese with English abstract).

Xu, W.L., Hergt, J.M., Gao, S., Pei, F.P., Wang, W., Yang, D.B., 2008. Interaction of adakitic melt–peridotite: Implications for the high-Mg$^{\#}$ signature of Mesozoic adakitic rocks in the eastern North China Craton. Earth and Planetary Science Letters 265, 123–137.

Xu, Y.G., Li, H.Y., Pang, C.J., He, B., 2009. On the timing and duration of the destruction of the North China Craton. Chinese Science Bulletin 54, 3379–3396.

Yan, J., Zhang, X., Chen, J.F., Zhao, H.L., 2001. Sr, Nd Isotopic characteristics of the Jinan Gabbro intrusion. Bulletin of Mineralogy, Petrology and Geochemistry 20, 302–305 (in Chinese with English abstract).

Yang, C.H., 2007. Chronology and geochemistry of Mesozoic high-Mg diorites in Western Shandong: constraints on lithospheric evolution of the North China Craton. Ph.D. dissertation, Jilin University, Jilin, pp. 1–124 (in Chinese with English abstract).

Yang, J.H., Wu, F.Y., Chung, S.L., Wilde, S., Chu, M.F., 2004. Multiple sources for the origin of granites: geochemical and Nd/Sr isotopic evidence from the Gudaoling granite and its mafic enclaves, northeast China. Geochimica et Cosmochimica Acta 68, 4469–4483.

Yang, C.H., Xu, W.L., Yang, D.B., Liu, C.C., Liu, X.M., Hu, Z.C., 2005a. Petrogenesis of Mesozoic high-Mg diorites in western Shandong: evidence from chronology and petro-geochemistry. Journal of the China University of Geosciences 16, 297–308.

Yang, J.H., Chung, S.L., Wilde, S., Wu, F.Y., Chu, M.F., Lo, C., Fan, H.R., 2005b. Petrogenesis of post-orogenic syenites in the Sulu orogenic belt, east China: geochronological, geochemical and Nd–Sr isotopic evidence. Chemical Geology 214, 99–125.

Yang, J.H., Wu, F.Y., Chung, S.L., Wilde, S.A., Chu, M.F., 2006. A hybrid origin for the Qianshan A-type granite, northeast China: geochemical and Sr–Nd–Hf isotopic evidence. Lithos 89, 89–106.

Yang, J.H., Wu, F.Y., Wilde, S.A., Xie, L.W., Yang, Y.H., Liu, X.M., 2007a. Tracing magma mixing in granite genesis: in situ U–Pb dating and Hf-isotope analysis of zircons. Contributions to Mineralogy and Petrology 153, 177–190.

Yang, J.H., Wu, F.Y., Xie, L.W., Liu, X.M., 2007b. Petrogenesis and tectonic implications of Kuangdonggou syenites in the Liaodong Peninsula, east North China Craton: constraints from in-situ zircon U–Pb ages and Hf isotopes. Acta Petrologica Sinica 23 (2), 263–276 (in Chinese with English abstract).

Yang, C.H., Xu, W.L., Yang, D.B., Wang, W., Wang, W.D., Liu, J.M., 2008. Petrogenesis of Shangyu gabbro-diorites in western Shandong: geochronological and geochemical evidence. Science in China (Series D) 51 (4), 481–492.

Yaxley, G.M., 2000. Experimental study of the phase and melting relations of homogeneous basalt plus peridotite mixtures and implications for the petrogenesis of flood basalts. Contributions to Mineralogy and Petrology 139, 326–338.

Ying, J.F., Zhou, X.H., Zhang, H.F., 2004. Geochemical and isotopic investigation of the Laiwu–Zibo carbonatites from western Shandong Province, China and implications for their petrogenesis and enriched mantle source. Lithos 75, 413–426.

Yogodzinski, G.M., Kay, R.W., Volynets, O.N., Koloskov, A.V., Kay, S.M., 1995. Magnesian andesite in the western Aleutian Komandorsky region: implications for slab melting and processes in the mantle wedge. Geological Society of America Bulletin 107, 505–519.

Zhai, M.G., 2008. Lower crust and lithospheric mantle beneath the North China Craton before the Mesozoic lithospheric disruption. Acta Petrologica Sinica 24, 2185–2204 (in Chinese with English abstract).

Zhai, M.G., Meng, Q.R., Liu, J.M., Hou, Q.L., Hu, S.B., Li, Z., Zhang, H.F., Liu, W., Shao, J.A., Zhu, R.X., 2004a. Geological features of Mesozoic tectonic regime inversion in Eastern North China and implication for geodynamics. Earth Science Frontiers 11, 285–297 (in Chinese with English abstract).

Zhai, M.G., Zhu, R.X., Liu, J.M., Meng, Q.R., Hou, Q.L., Hu, S.B., Liu, W., Li, Z., Zhang, H.F., Zhang, H.F., 2004b. Time range of Mesozoic tectonic regime inversion in eastern North China Block. Science in China (Series D) 47, 151–159.

Zhai, M.G., Fan, Q.C., Zhang, H.F., Sui, J.L., Shao, J.A., 2007. Lower crustal processes leading to Mesozoic lithospheric thinning beneath eastern North China: underplating, replacement and delamination. Lithos 96, 36–54.

Zhang, Y.Q., Dong, S.W., 2008. Mesozoic tectonic evolution history of the Tan-Lu fault zone, China: advances and new understanding. Geological Bulletin of China 27, 1371–1390 (in Chinese with English abstract).

Zhang, H.F., Sun, M., 2002. Geochemistry of Mesozoic basalts and mafic dikes, southeastern North China Craton, and tectonic implications. International Geology Review 44, 370–382.

Zhang, H.F., Sun, M., Zhou, X.H., Fan, W.M., Zhai, M.G., Yin, J.F., 2002. Mesozoic lithosphere destruction beneath the North China Craton: evidence from major-, trace-element and Sr–Nd–Pb isotope studies of Fangcheng basalts. Contributions to Mineralogy and Petrology 144, 241–253.

Zhang, Y.Q., Dong, S.W., Shi, W., 2003. Cretaceous deformation history of the middle Tan-Lu fault zone in Shandong Province, eastern China. Tectonophysics 363, 243–258.

Zhang, H.F., Sun, M., Zhou, M.F., Fan, W.M., Zhou, X.H., Zhai, M.G., 2004. Highly heterogeneous Late Mesozoic lithospheric mantle beneath the North China Craton: evidence from Sr–Nd–Pb isotopic systematics of mafic igneous rocks. Geological Magazine 141, 55–62.

Zhang, H.F., Sun, M., Zhou, X.H., Ying, J.F., 2005a. Geochemical constraints on the origin of Mesozoic alkaline intrusive complexes from the North China Craton and tectonic implications. Lithos 81, 297–317.

Zhang, H.F., Zhou, X.H., Fan, W.M., Sun, M., Guo, F., Ying, J.F., Tang, Y.J., Zhang, J., Niu, L.F., 2005b. Nature, composition, enrichment processes and its mechanism of the Mesozoic lithospheric mantle beneath the southeastern North China Craton. Acta Petrologica Sinica 21, 1271–1280 (in Chinese with English abstract).

Zhang, X.M., Zhang, Y.Q., Ji, W., 2007. Fault distribution patterns of the Luxi Block, Shandong, and Mesozoic sedimentary–magmatic-structural evolution sequence. Journal of Geomechanics 13, 163–172 (in Chinese with English abstract).

Zhang, X.H., Zhang, H.F., Jiang, N., Zhai, M.G., Zhang, Y.B., 2010. Early Devonian alkaline intrusive complex from the northern North China Craton: a petrological monitor of post-collisional tectonics. Journal of the Geological Society 167, 717–730.

Zhao, J.X., Shiraishi, K., Ellis, D.J., Sheraton, J.W., 1995. Geochemical and isotopic studies of syenites from the Yamoto Mountains, East Antartica: implication for the origin of syenitic magmas. Geochimica et Cosmochimica Acta 59, 1363–1385.

Zhao, G.C., Wilde, S.A., Cawood, P.A., Sun, M., 2001. Archean blocks and their boundaries in the North China Craton: lithological, geochemical, structural and P–T path constraints and tectonic evolution. Precambrian Research 107, 45–73.

Zhao, G.C., Sun, M., Wilde, S.A., Li, S.Z., 2005. Late Archean to Paleoproterozoic evolution of the North China Craton: key issues revisited. Precambrian Research 136, 177–202.

Zheng, J.P., 2009. Comparison of mantle-derived materials from different spatiotemporal settings: implications for destructive and accretional processes of the North China Craton. Chinese Science Bulletin 54, 3397–3416.

Zhou, X.H., Sun, M., Zhang, G.H., Chen, S.H., 2002. Continental crust and lithospheric mantle interaction beneath North China: isotopic evidence from granulite xenoliths in Hannuoba, Sino-Korean craton. Lithos 62, 111–124.

Zhu, R.X., Zheng, T.Y., 2009. Destruction geodynamics of the North China Craton and its Paleoproterozoic plate tectonics. Chinese Science Bulletin 54, 3354–3366.

Zhu, G., Song, C.Z., Niu, M.L., Liu, G.S., Wang, Y.S., 2002. Lithospheric textures of the Tan-Lu Fault Zone and their genetic analysis. Geological Journal of China Universities 8, 248–256 (in Chinese with English abstract).

Zhu, G., Liu, G.S., Niu, M.L., Song, C.Z., Wang, D.X., 2003. Transcurrent movement and genesis of the Tan-Lu fault zone. Geological Bulletin of China 22, 200–207 (in Chinese with English abstract).

Zindler, A., Hart, S.R., 1986. Chemical geodynamics. Annual Review of Earth and Planetary Sciences 14, 493–571.

Zou, H.B., Zindler, A., Xu, X.S., Qi, Q., 2000. Major, trace element, and Nd, Sr and Pb isotope studies of Cenozoic basalts in SE China: mantle sources, regional variations, and tectonic significance. Chemical Geology 171, 33–47.